Dynamical Downscaling of the Climate for the Hawaiian Islands. Part I: Present-day

4 authors:

Chunxi Zhang
University of Hawai'i System
12 PUBLICATIONS **177** CITATIONS

SEE PROFILE

Yuqing Wang
University of Hawaiʻi at Mānoa
161 PUBLICATIONS **4,877** CITATIONS

SEE PROFILE

Kevin Hamilton
University of Hawaiʻi at Mānoa
126 PUBLICATIONS **4,625** CITATIONS

SEE PROFILE

Axel Lauer
University of Hawaiʻi at Mānoa
65 PUBLICATIONS **2,750** CITATIONS

SEE PROFILE

Dynamical Downscaling of the Climate for the Hawaiian Islands. Part I: Present Day

CHUNXI ZHANG, YUQING WANG, KEVIN HAMILTON, AND AXEL LAUER*

International Pacific Research Center, and Department of Atmospheric Sciences, School of Ocean and Earth Science and Technology, University of Hawai'i at Mānoa, Honolulu, Hawaii

ABSTRACT

Hawaii's high and steep topography leads to pronounced small-scale variations in climate, and this makes comprehensive modeling of the weather and climate particularly challenging. This paper describes a regional model formulation designed for simulations of the microclimates in Hawaii and then documents and analyzes an extended retrospective simulation for near-present-day conditions. Part II will apply the model to projected climate conditions near the end of the present century.

A nested version of the Advanced Research version of the Weather Research and Forecasting Model with fine horizontal resolution and improved physics for the Hawaiian region has been configured. A 20-yr triply nested simulation of the atmospheric flow was undertaken with a 3-km-resolution mesh covering all main Hawaiian Islands and a 1-km mesh over Maui. Ocean surface temperatures are prescribed from observations, and meteorological fields at the boundaries of the outermost domain are taken from global reanalyses. The simulations are compared to surface, balloon, and satellite observations over the same period. The 3-km version of the model realistically simulates the frequency of trade wind inversions, time-mean rainfall, and other variables on relatively small scales over the island of Hawaii. There is a reasonable agreement between observed and simulated mean rainfall patterns over the other islands as well. However, the simulated distribution of mean rainfall over Kauai and (most particularly) Maui and Oahu reveals some significant deficiencies, which is attributed to inadequate resolution of the topography on these islands. The 1-km simulation over Maui shows clear improvement in the mean rainfall over the 3-km version.

1. Introduction

The application of limited-area dynamical atmospheric models to simulate fields at fine horizontal scales that are consistent with coarser-scale global analyses or global general circulation model (GCM) simulations is being actively pursued for many geographical areas around the world (e.g., Laprise et al. 1998; Wang et al. 2004; Fu et al. 2005; Rummukainen 2010; Mearns et al. 2012; Rasmussen et al. 2014; Mahoney et al. 2013). Much of the current interest is motivated by the desire to provide local-scale climate change projections consistent with global coupled ocean–atmosphere model results (e.g.,

Mearns et al. 2012). This ''dynamical downscaling'' via regional comprehensive models is also potentially useful for seasonal climate prediction. In addition, retrospective simulations with limited-area models forced by observed boundary conditions could find application in understanding and modeling the finescale dependence of aspects of the local environment such as groundwater availability, nutrient deposition to the soil, the ecology of plant communities, and so forth.

Regularly gridded global reanalyses of the observed atmospheric fields are now produced by several major meteorological centers throughout the world, and generally such gridded fields are made available at $\sim$(50–300)-km horizontal spacing. The $\sim$(50–300)-km grid spacing is also typical of the global coupled models now being run for long-term climate projections (e.g., Taylor et al. 2012). For many locations and particular applications, there is some interest in dynamically downscaled fields at even only moderately finer resolution. For example, the U.S. multi-agency North American Regional Climate Change Assessment Program (NARCCAP) involves downscaling

* Current affiliation: DLR Institute of Atmospheric Physics, Oberpfaffenhofen, Germany.

Corresponding author address: Dr. Yuqing Wang, International Pacific Research Center, SOEST, University of Hawai'i at Mānoa, 1680 East-West Road, Honolulu, HI 96822.
E-mail: yuqing@hawaii.edu

a large number of coupled global model projections for the North American region using several regional atmospheric models run at about 50-km horizontal resolution (Mearns et al. 2012). A somewhat similar program [referred to as USGS Regional Climate Downscaling (RegCLIM)] led by the U.S. Geological Survey is producing downscaled climate projections for large parts of North America using a regional model with ~15-km horizontal resolution (Hostetler et al. 2011). While such dynamical downscaling datasets may be valuable for many regions, they would have very little applicability to the Hawaiian Islands, where the unusual geography results in very finescale microclimatic gradients.

State-of-the-art global models with a horizontal resolution of ~100 km or coarser may represent all the Hawaiian Islands as just a handful of land grid boxes. Without an adequate representation of the very high and steep topographic relief characteristic of Hawaii, such models cannot simulate even basic features of the winds, temperature, and rainfall over the Hawaiian Islands. Notably, even a first-order representation of the observed intra-island geographical distribution of rainfall clearly requires using a model with much finer resolution than those now employed in the NARCCAP or USGS RegCLIM downscaling exercises.

In their recent review, Harter et al. (2015) provide an overview on the impacts of global climate change on the flora of oceanic islands. Even though the authors emphasize the importance and the need for more and better climate data and models on the island scale, only very few studies applying very high-resolution dynamical downscaling for the oceanic islands exist at present. Examples of such studies include, for instance, Morel et al. (2014) who documented the capabilities of the Advanced Research version of the Weather Research and Forecasting (WRF) Model (e.g., Skamarock et al. 2008) to simulate rainfall at very fine (680 m) spatial resolution over La Réunion. Similar to Hawaii, La Réunion is a small volcanic island with complex topography and a tropical maritime climate with two marked seasons. Pérez et al. (2014) evaluated the WRF parameterizations for dynamical downscaling in the Canary Islands with a horizontal resolution of up to 5 km. This study showed that specific model configurations were able to reproduce observations of important variables in this archipelago reasonably well, demonstrating the potential for regional climate change simulations. Kendon et al. (2014) used a multiply nested regional atmospheric model to downscale a global GCM climate simulation for a region in southern England and employed an inner grid with 1.5-km resolution. The application of very high-resolution regional models has been reviewed recently by Prein et al. (2015).

Zhang et al. (2012a, hereafter ZWLH) configured a nested version of the WRF Model with both fine resolution (3 km) and improved physics appropriate for the Hawaiian region. We follow ZWLH and refer to this as the Hawaiian regional climate model (HRCM). Configuring the HRCM involved several modifications of the publicly available WRF versions. Notably the HRCM includes a version of the Tiedtke convection parameterization scheme implemented as described by Zhang et al. (2011), which has been made publicly available and is now part of the standard WRF since version 3.3. The HRCM was then further improved by including a modified cloud microphysics package and introducing a detailed specification of surface properties (albedo, land-cover type, soil type, and green vegetation fraction) for the Hawaiian Islands (ZWLH). ZWLH discussed a 1-yr retrospective simulation (November 2005–October 2006) in a doubly nested version at horizontal resolutions of 15 and 3 km over the main Hawaiian Islands and the surrounding ocean region. This retrospective integration was driven with observed daily sea surface temperature (SST) and horizontal boundary fields taken from global meteorological reanalyses. Since then we have completed a 20-yr retrospective simulation (1990–2009) and a 20-yr simulation driven with projected future conditions representing the end of the current century (2080–99). These new model integrations employed a triply nested version of HRCM that included a 1-km grid mesh over the island of Maui and adjacent ocean regions.

The present paper is Part I of a two-part series and reports on the 20-yr retrospective simulation, while Part II will discuss the projected late twenty-first-century climate change simulation. Part II will also discuss some of the specific motivations for producing fine-resolution climate projections for Hawaii. Note that Leong et al. (2014) provide an up-to-date review of many aspects of climate change impacts seen and anticipated in Hawaii.

This first paper will demonstrate that the HRCM performs well enough in simulating present-day microclimatic conditions that it can be applied reasonably in projecting the fine structure of climate changes on individual islands. An important aim of the present paper is to improve our knowledge of the advantages and limitations of high-resolution dynamical downscaling with a regional climate model applied to the Hawaiian Islands. Specifically, we (i) investigate the effect of improving the 3-km horizontal resolution employed by ZWLH and exploring the behavior of an atmospheric model in extended simulations at 1-km resolution; (ii) provide a 20-yr simulation that allows more-reliable statistics to be computed for comparisons with observations of various kinds, notably for rainfall, including

its diurnal variation; (iii) evaluate how well the interannual variations in rainfall and other quantities over individual locations can be captured by a high-resolution model forced by observed SSTs and large-scale boundary fields; and (iv) provide a first comparison of the regional geographical modulation of the boundary layer structure simulated in a high-resolution model with that derived recently from satellite radio occultation data (Zhang et al. 2012b).

The paper is organized as follows. Section 2 briefly outlines some dominant features of the present-day atmospheric circulation and climate for Hawaii. Section 3 describes the observational datasets that we have used for evaluating the model results and briefly summarizes the basic HRCM description from ZWLH and lays out the details of the configuration adopted for the present simulation. Sections 4 and 5 describe aspects of the simulation in the HRCM outermost and intermediate domains, respectively. Section 6 examines the simulation over Maui in the 1-km-resolution innermost domain. Results are discussed and conclusions are summarized in section 7.

2. Meteorological background

The atmospheric general circulation sets the stage for any study of Hawaiian climate. Much of the subtropics and adjacent tropical regions are dominated by a mean sinking motion through the troposphere. Over the continents this leads to the familiar subtropical deserts, while over much of the tropical and subtropical oceans the large-scale circulation establishes a regime typified by a well-mixed marine boundary layer (MBL) capped by a temperature inversion layer. Around Hawaii over 80% of atmospheric soundings can be characterized as having well-defined trade wind inversions (TWIs), which cap the MBL at heights ranging from 1000 to 4000 m above sea level (Cao et al. 2007). Typically, the TWI layer is about 300 m thick and the relative humidity drops by ~40% across this layer (Cao et al. 2007). The prevailing surface winds in Hawaii are from the east-northeast, and, generally speaking, days with a well-defined TWI also tend to have surface winds with an easterly component.

For the characterization of Hawaii climate, it is useful to divide the year into the cooler, rainier half (winter, which we define throughout this paper as November through April) and the warmer, drier half (summer, May through October). Rainfall directly over the main Hawaiian Islands is generally heavier than over adjacent ocean areas as a result of the strong interaction between the topography and boundary layer flow (e.g., Schroeder 1993). During the dominant trade wind weather patterns there is generally abundant orographic rain along the northeastward-facing slopes and very pronounced rain shadows over most of the "leeward" (i.e., leeward relative to the mean trade winds) sides of the islands (Lyons 1982). Under the usual TWI conditions there is rarely much deep convective rain over the islands. However, deep convection can occur when the usual TWI pattern is absent. Each winter (and occasionally in summer), the trade wind weather is disrupted several times by spells of more disturbed weather, notably frontal passages or other effects associated with cyclones centered at higher latitudes. On occasion the usual circulation pattern right around Hawaii is strongly perturbed by slowly moving, closed low pressure circulations (so-called Kona lows), which may persist in the vicinity for several days or even longer. These disturbed conditions lead to days without clearly defined TWI and often feature convective rain. These non-TWI, convective rain events account for much of the total rainfall that falls on the normally dry leeward areas in the islands. In summer, tropical depressions and tropical cyclones can lead to very heavy rainfall events, but close encounters of such tropical disturbances with the main Hawaiian Islands are relatively infrequent (Chu and Clark 1999). Figure 1a shows schematically some of the key processes governing the rainfall in Hawaii.

3. Observations and model description

In this section, we first describe the data employed to evaluate the model simulation, including in situ and remote sensing observations as well as gridded analyses derived from observations, and then present the model integration performed.

a. Balloon soundings

For the entire 1990–2009 period the National Weather Service conducted twice-daily operational balloon soundings near the eastern and western extremes of the main Hawaiian Islands, namely at Hilo Airport on Hawaii island (which we will refer to here as the Big Island) and at Lihue Airport on Kauai (Fig. 1b). The soundings include air temperature, humidity, and wind speed. Typically, there are around 35 levels with data reported below 600 hPa with the density of reports enhanced through the inversion layer itself. The data are available online (http://weather.uwyo.edu/upperair/sounding.html).

b. Surface observations

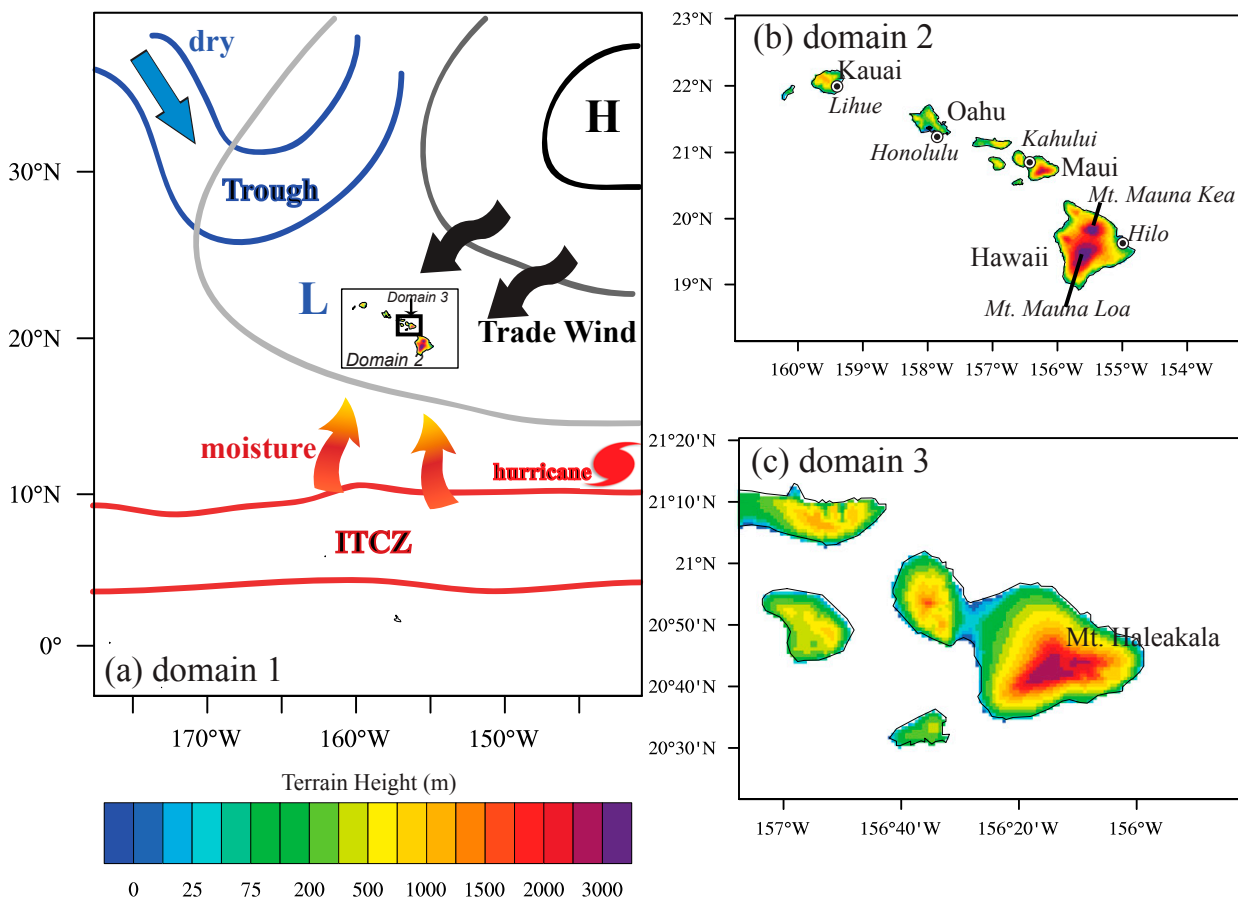There are several surface weather stations at airports (METAR stations) throughout the islands. We will

FIG. 1. (a) Model domains and synoptic patterns most relevant to weather and climate in the Hawaiian Islands. (b) Domain 2 and the terrain heights and the locations of the METAR stations employed here. (c) Domain 3 (1-km horizontal resolution).

focus on the detailed observations from METAR stations on each of the four largest islands: Lihue on Kauai, Honolulu on Oahu, Kahului on Maui, and Hilo on the Big Island (see Fig. 1b and the stations denoted by bold type in Table 1). Hourly observations of several variables are taken at each of these stations and the data are available online from the U.S. National Centers for Environmental Information (NCEI) website (https://www.ncei.noaa.gov). For comparisons with the model results we will use the station observations of surface air temperature (SAT), surface wind, rainfall, and surface specific humidity (Q_2). The surface wind reported in the METAR data is a 2-min average of the wind at 10-m height above ground (www.nws.noaa.gov/om/tpb/474body.htm). The hourly METAR data are used to construct daily and monthly means.

In addition to the METAR stations, NCEI records daily observations from over 50 cooperative weather stations in the main Hawaiian Islands (http://www.prh.noaa.gov/data/HFO/RRMHFO). We used the SAT data (as monthly means reported by the NCEI) from each of the 43 stations for which monthly SAT means

were reported for at least 50% of the months during 1990–2009. We also included SAT observations from an additional station at the summit of Mauna Kea on the Big Island that are reported by the Mauna Kea Weather Center (http://mkwc.ifa.hawaii.edu/archive/index.cgi). (The network of stations is shown in Fig. 11a and details are given in Table 1.)

Rainfall amounts are known to exhibit very sharp horizontal contrasts in Hawaii and so characterizing the observed rainfall climatology from observations is challenging. The Rainfall Atlas of Hawaii project (Giambelluca et al. 2013; Frazier et al. 2016) has tried to compile all available rainfall observations and interpolate them to produce observed monthly mean rainfall rates at a nominal 250-m resolution over the Hawaiian Islands. The number of rain gauge stations available generally declines over the years, but in 2012, for example, monthly data at 404 stations (maintained by various organizations) were available. Frazier et al. (2016) discuss results from different Kriging approaches for their interpolation using topographic height as a secondary variable. They selected what they judged as the best

TABLE 1. Long-term mean SAT from the METAR (in boldface) and other surface temperature stations (some of the stations are shown in Fig. 11). Also shown is the difference ΔSAT with the model simulation using values interpolated horizontally to the station location. The quantity ΔElev is the elevation difference between the model-interpolated topography and the actual station elevation. SAT adj is the air temperature adjustment applied to the model result to account for this elevation bias. The last column shows the ΔSAT after the elevation-related adjustment (adj).

Station name	Lat (°N)	Lon (°E)	Elev (m)	ΔElev (m)	SAT (°C)	ΔSAT (°C)	SAT adj (°C)	ΔSAT after adj (°C)
Camp Erdman	21.6	−158.2	2.1	182.9	24.1	−1.9	1.2	−0.8
Glenwood number 2	19.5	−155.1	670.6	−75.9	19.5	−1.1	−0.5	−1.6
Haleakala ranger station 338	20.8	−156.2	2121.4	168.7	12.5	−3.3	1.1	−2.2
Hana Airport	20.8	−156.0	22.9	55.6	23.3	−0.3	0.4	0.0
Hawaii Vol National Park HQ 54	19.4	−155.2	1210.4	−72.5	16.5	−1.6	−0.5	−2.0
Hilo International Airport	**19.7**	**−155.1**	**11.6**	**-2.5**	**23.4**	**0.7**	**-0.0**	**0.7**
Honolulu Observatory	21.3	−158.0	0.9	0.0	24.5	−0.2	0.0	−0.2
Honolulu International Airport	**21.3**	**−157.9**	**2.5**	**3.0**	**25.5**	**−0.7**	**0.0**	**−0.7**
Kahoolawe	20.5	−156.6	365.8	−104.3	21.9	0.2	−0.7	−0.5
Kahului Airport	**20.9**	**−156.4**	**15.5**	**23.1**	**24.4**	**−0.6**	**0.2**	**−0.4**
Kailua 446	20.9	−156.2	213.4	7.7	20.0	1.2	0.1	1.3
Kainaliu	19.5	−155.9	457.2	37.9	20.8	−0.1	0.2	0.2
Kanalohuluhulu	22.1	−159.6	1097.3	−111.0	15.0	1.4	−0.7	0.6
Kaneohe	21.4	−157.8	14.6	34.4	25.1	−1.2	0.2	−1.0
Kapalua West Maui Airport	21.0	−156.7	73.2	62.2	24.2	−0.9	0.4	−0.5
KE Ahole Point	19.7	−156.1	6.1	11.5	24.9	−0.3	0.1	−0.2
Kihalani	20.0	−155.2	301.8	−42.6	21.7	−0.3	−0.3	−0.6
Kii Kahuku 911	21.7	−157.9	7.6	4.6	24.2	−0.3	0.0	−0.3
Kula branch station	20.8	−156.3	944.9	72.1	17.8	−0.4	0.5	0.1
Kula hospital 267	20.7	−156.4	923.5	207.4	17.4	−1.2	1.3	0.2
Kulani camp 79	19.5	−155.3	1575.8	−32.8	12.8	−0.4	−0.2	−0.6
Lanai Airport	20.8	−156.9	396.2	−42.3	21.9	−0.7	−0.3	−1.0
Lihue Airport	**22.0**	**−159.3**	**54.0**	**−19.1**	**24.3**	**−0.7**	**−0.1**	**−0.8**
Makaha country club	21.5	−158.2	76.2	158.6	24.1	−1.8	1.0	−0.7
Makena golf course	20.6	−156.4	26.8	83.8	24.0	−0.4	0.5	0.2
Makaweli	21.9	−159.6	42.7	−9.8	24.5	−1.2	−0.1	−1.2
Manoa Lyon Arbo	21.3	−157.8	152.4	106.4	22.7	−0.7	0.7	−0.0
Mauna Loa slope OBS 39	19.5	−155.6	3398.5	96.4	8.0	−1.8	0.6	−1.2
Molokai Airport	21.1	−157.1	135.0	9.0	23.7	−0.9	0.1	−0.8
Naalehu	19.0	−155.6	245.7	−77.8	22.7	−0.1	−0.5	−0.6
OHE'O	20.6	−156.0	28.0	2.4	24.0	−0.1	0.0	−0.1
Opihihale	19.3	−155.9	414.5	70.9	20.9	0.2	0.5	0.7
Princeville Ranch	22.2	−159.5	66.1	−33.2	23.5	−0.1	−0.2	−0.4
Puukolii	20.9	−156.7	128.0	37.2	24.0	−0.5	0.2	−0.3
Puukohola Heiau	20.0	−155.8	40.5	39.0	23.4	1.2	0.3	1.4
Puu Manawahua	21.4	−158.1	509.9	−288.8	21.2	1.1	−1.9	−0.7
Sea Mountain	19.1	−155.5	24.4	−6.2	23.6	0.4	−0.0	0.4
South Kona 2	19.1	−155.8	719.3	1.1	19.6	−0.2	0.0	−0.2
Upper Wahiawa	21.5	−158.0	306.9	−52.0	22.1	−0.3	−0.3	−0.7
Waikiki	21.3	−157.8	3.0	18.5	25.1	−0.7	0.1	−0.6
Waimanalo experimental farm	21.3	−157.7	19.5	43.1	24.2	−0.7	0.3	−0.5
Waimea arboretum 892	21.6	−158.1	12.5	121.8	23.7	−1.1	0.8	−0.3
Waimea 947	22.0	−159.7	6.1	20.3	23.9	−0.0	0.1	0.1
Mauna Kea summit	19.8	−155.5	4205.0	−350.0	2.2	1.7	−2.3	−0.5

approach to produce the monthly gridded values that are available online (http://rainfall.geography.hawaii.edu, where maps of the station locations can also be found). For our project we aggregated the 250-m observed data to the HRCM 3- and 1-km grids implemented by using the patch interpolation in NCAR Command Language (https://www.ncl.ucar.edu).

The Rainfall Atlas of Hawaii does not include hourly data, but we will compare the observed and modeled diurnal cycle of rainfall. For this we use hourly rain gauge measurements from the NCEI hourly precipitation dataset and also from the National Weather Service Hydronet, which has been recording 15-min rainfall amounts at stations in Hawaii since 1995

(http://www.prh.noaa.gov/hnl/hydro/hydronet/hydronet-data.php). After a data consistency and quality check, we chose 109 stations from the NCEI dataset from 1995 to 2009. During the same time period, there are 64 Hydronet stations available. We performed a Cressman interpolation (Cressman 1959) of the hourly precipitation data onto the domain 2 3-km grids (following ZWLH). The observed hourly data used are all from 1995–2009; the comparisons presented later concerning the diurnal cycle of rainfall are computed using the model integration for the same 15-yr period. As an aside, we evaluated our simple Cressman interpolation by comparing our interpolated long-term mean rainfall with the more sophisticated results of Frazier et al. (2016) and found generally only small differences.

c. Satellite observations

The MBL structure is measured in situ only by the operational balloon soundings at Hilo and Lihue (see section 3a above), but Zhang et al. (2012b) reported on the use of satellite remote sensing data in determining the TWI base heights above sea level (TWIBH) in the Hawaiian region. The moisture and temperature gradient across the base of the TWI layer results in a sharp radio refractivity gradient that can be detected by the global positioning system (GPS) radio occultation (RO) measurements (e.g., Sokolovskiy et al. 2006; Guo et al. 2011; Xie et al. 2012). Zhang et al. (2012b) employed an algorithm to identify the TWIBH from RO soundings (following the method of Guo et al. 2011) and then constructed a climatological map of mean TWIBH for the Hawaiian region interpolated from all the individual observations from June 2006 to December 2010. Note that the interpolated TWIBH is smoothed to an effective horizontal resolution of ~25 km (this is a particular limitation in representing the inversion base heights over the mountain peaks on the Big Island).

The Global Precipitation Climatology Project (GPCP) monthly precipitation dataset version 2.2 is used to evaluate the precipitation in the outermost domain of the HRCM. This dataset consists of monthly means of precipitation derived from satellite and rain gauge measurements (Adler et al. 2003) and is available at 2.5° latitude–longitude resolution. We also employed the monthly mean gridded Tropical Rainfall Measuring Mission (TRMM) precipitation 3B43 product with 0.25° resolution based on TRMM and other satellite observations for the time period 1998–2009 (Huffman et al. 2007).

d. Model and integration

A more detailed description of the HRCM can be found in ZWLH. The grid configuration used in the present study is shown in Fig. 1. The model uses one-way nesting, and domains 1, 2, and 3 are integrated with 15-, 3-, 1-km grids on a Mercator projection. The outer 15 grid points in domain 1 are used as a buffer zone in which the results are relaxed to values interpolated in time and space from the 6-h snapshots provided by the NASA MERRA reanalyses (Rienecker et al. 2011). The SST is prescribed and updated daily using the 0.25° × 0.25° NOAA global analysis described by Reynolds et al. (2010) (see ZWLH for our treatment of the diurnal variability of the SST). The model integrations started at 0000 UTC 1 January 1990 and ended on 0000 UTC 1 January 2010. We analyze the whole record without discarding a "spinup" period, since the initial soil moisture and temperature are not crucial to the model performance over the Hawaiian Islands. The model runs in domains 1, 2, and 3 were performed with time steps of 75, 15, and 5 s, respectively. The soil moisture and soil temperature at the initial time are taken from the European Centre for Medium-Range Weather Forecasts (ECMWF) interim reanalysis (ERA-Interim) data with a resolution of 0.75° × 0.75° (Dee et al. 2011). The initial conditions for the atmosphere were interpolated from the MERRA global reanalyses (0.5° × 0.67°).

Practical constraints limited us to a single realization of the 20-yr period simulated. In fact, we can expect this integration to be impacted by random high-frequency internal variability as well as variations under the control of the imposed observed SSTs and lateral boundary conditions (e.g., Cretat et al. 2011). We cannot expect the observed day-to-day evolution of the weather, particularly at small spatial scales, to be reproduced, but, in principle, the seasonal and longer-scale interannual variations may be reasonably captured in a single model realization if the control by imposed boundary forcing is sufficiently strong. At least it is meaningful to ask if the model does simulate the interannual variations of the local climate. We show in section 5 that the model does indeed do a reasonable job in simulating the interannual variability on seasonal time scales.

4. Outermost domain simulation

Figure 2 compares our simulated 20-yr mean precipitation in domain 1 with GPCP observations for the same period. In winter, the domain-averaged precipitation is 2.81 mm day^{-1}, which is smaller than 3.30 mm day^{-1} indicated by GPCP (Figs. 2a,b). The spatial correlation (SC) between the simulation and GPCP observations computed on the 15-km domain 1 grid is 0.94. In summer (Figs. 2c,d) the domain-averaged simulated precipitation is 2.56 mm day^{-1}, about 6.5% smaller than the value computed from the GPCP data (2.74 mm day^{-1}). The SC between the simulation and GPCP observations is 0.96.
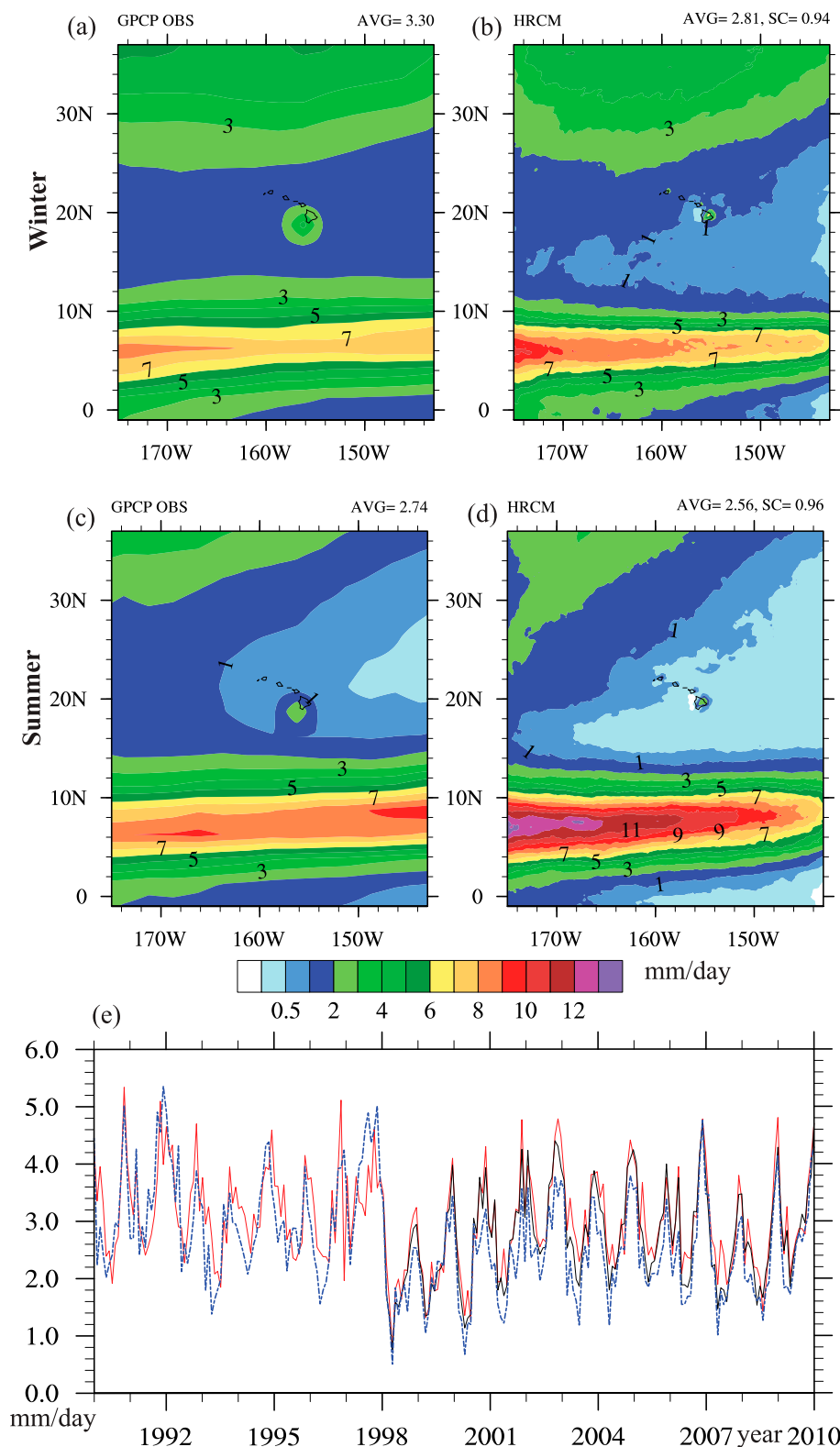
FIG. 2. The 20-yr mean winter precipitation in the (a) GPCP gridded observations and (b) HRCM 15-km simulation. (c),(d) As in (a),(b), but for summer, respectively. The black numbers in (a)–(d) label the contour lines. AVG means domain averaged precipitation, and SC means spatial correlation. (e) The time series for the simulated monthly mean rainfall averaged over the whole domain in the model simulation (dashed blue), the GPCP observations (red), and the TRMM observations (black). SC means spatial correlation coefficient.
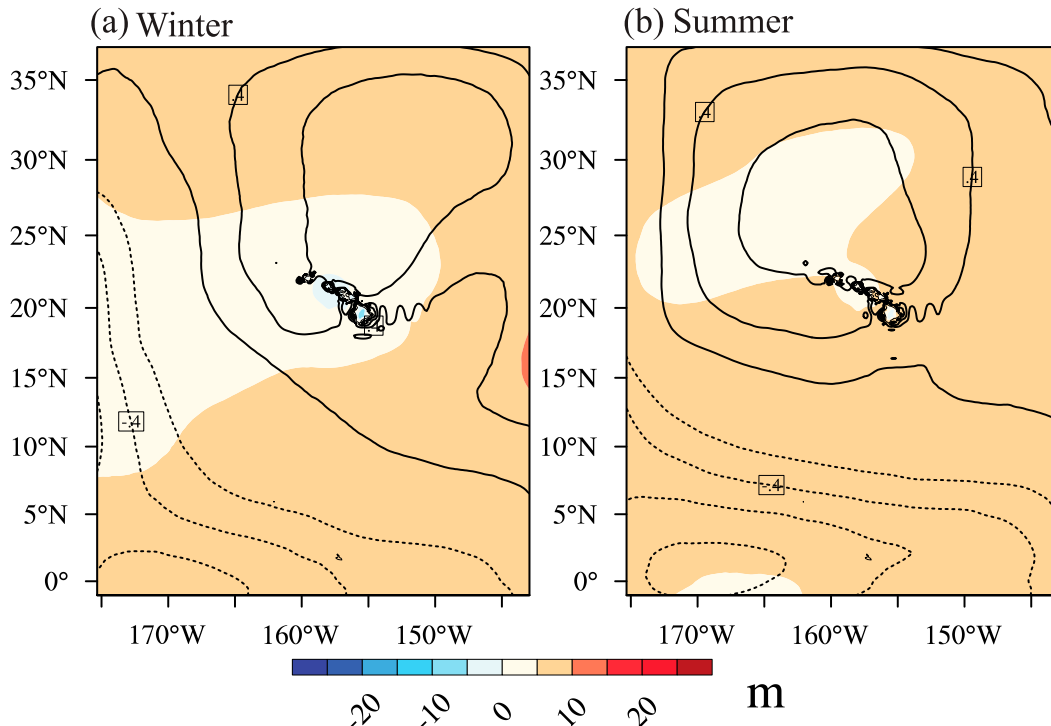
FIG. 3. The 20-yr mean GHT500 (shaded; m) and mean SLP (contours; hPa) biases (HRCM simulation − MERRA reanalysis data) for (a) winter and (b) summer.

In both seasons the simulated mean precipitation rate is larger than that observed in the ITCZ and less than that observed near, and to the east of, the Hawaiian Islands. Figure 2e shows the monthly time series of domain-averaged precipitation in the HRCM simulation compared with those computed from the GPCP and TRMM rainfall datasets. The main features of the annual cycle as well as the most prominent observed interannual variations (notably over 1997/98) are reasonably well simulated by the HRCM.

Figure 3 shows the biases in 20-yr means of simulated 500-hPa geopotential height (GHT500) and sea level pressure (SLP) compared with MERRA reanalyses for the same period. The biases are quite small (between −0.2 and 1.0 hPa in SLP and between −15 and 15 m in GHT500) and exhibit only very large-scale gradients (except for the region over the islands where the noisy-looking results presumably reflect differences in topography and the vertical interpolation/extrapolation between the model and MERRA values). The rather good simulation documented in Figs. 2 and 3 suggests that the regional model with realistic boundary forcing and prescribed SSTs can produce a reasonable representation of the regional-scale fields, even without interior large-scale nudging of model fields as has been done in many other regional climate simulations (e.g., Miguez-Macho

et al. 2004; Castro et al. 2005; Lo et al. 2008; Alexandru et al. 2009; Bowden et al. 2012).

5. Intermediate (3 km) domain simulation

a. Comparison with METAR station observations

The probability density functions (PDFs) of daily mean SAT, daily maximum SAT, daily minimum SAT, daily mean surface specific humidity Q_2, daily mean surface wind speed, and daily rainfall were computed over all days during 1990–2009 from the METAR station data and from the HRCM simulation results at the nearest land grid points to the station locations. The results are shown in Fig. 4 together with the 20-yr mean biases (HRCM simulation minus observations). Overall the PDFs in the HRCM simulation and observations are quite similar. The mean SAT biases are less than 0.7°C at all stations. The daily maximum and minimum SAT biases are slightly larger and are in the range of 0.06–1.84°C. The bias in humidity at both Lihue and Honolulu is quite small and the simulated PDFs at these stations are similar to the observed. The simulated Q_2 has a dry bias of ~2 g kg^{-1} at both Kahului and Hilo. The HRCM simulation has a surface wind speed bias of 1.59 m s^{-1} at Kahului, 0.43 m s^{-1} at Honolulu, and even smaller biases at Hilo and Lihue.
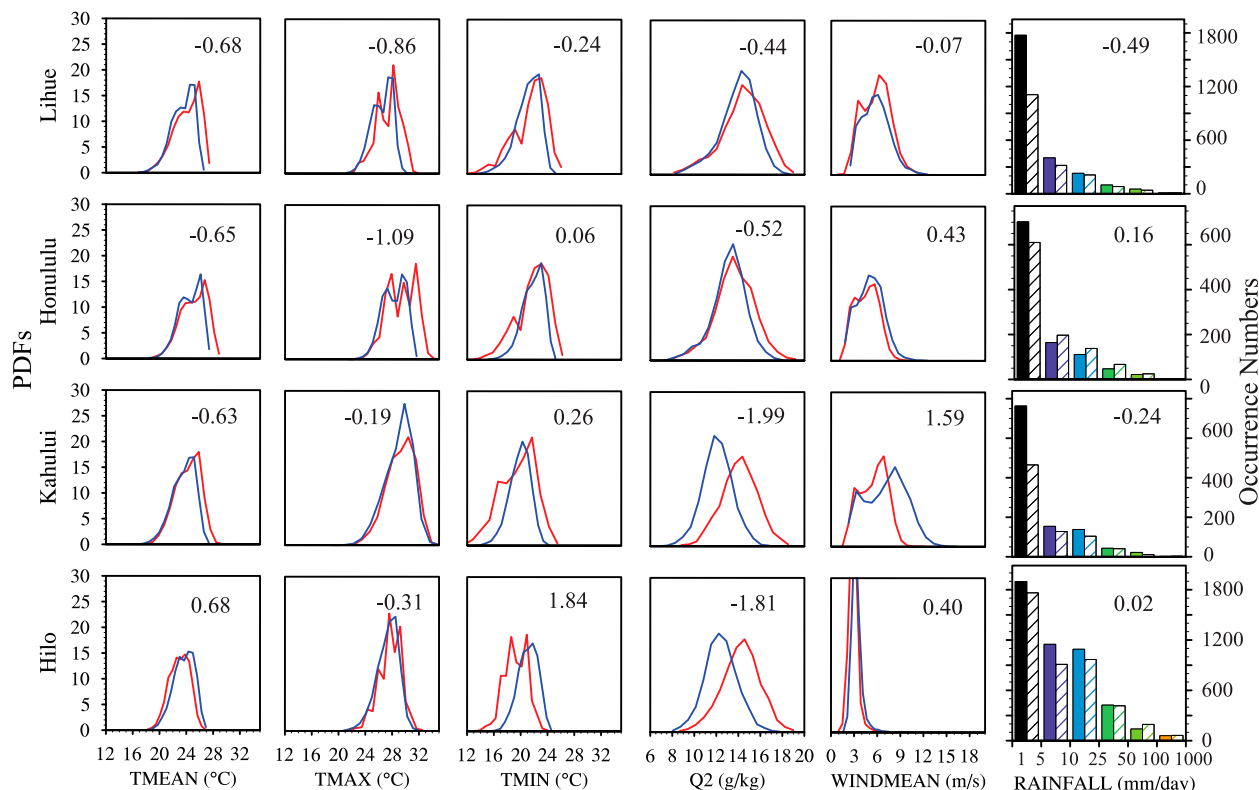
FIG. 4. PDFs of the daily values over the time period 1990–2009 of (left)–(right) daily mean SAT, daily maximum SAT, daily minimum SAT, daily mean Q_2, and daily mean surface wind speed at (top)–(bottom) Lihue, Honolulu, Kahului, and Hilo. Red lines show station observations and blue lines are for the HRCM 3-km simulation at nearest land grid points to stations. The simulated long-term mean biases (HRCM simulation − observations) for each variable are also shown in the figure. The rightmost column is the daily rainfall histogram for each station with colored shading showing the observed values and the hatching showing the result for the HRCM 3-km simulation. The bin width for SAT is 1°C, 1 g kg^{-1} for Q_2, 1 m s^{-1} for wind speed, and uneven for rainfall as shown by the tick marks.

The largest mean rainfall bias in the HRCM simulation among the stations is −0.49 mm day^{-1} for Lihue. The observed distribution of daily rainfall total at each of the stations is rather well captured in the HRCM simulation. The main disagreement is for light rainfall (1–5 mm day^{-1}) days, which are less frequent at Lihue and Kahului in the simulation than in the observations.

The long-term mean seasonal cycle in surface variables is presented as the 20-yr means for each calendar month for the same variables (Fig. 5) at the same locations as in Fig. 4. Correlation coefficients of the 12 observed and simulated values for each quantity are also shown in Fig. 5. In each case the seasonal cycle of these surface variables is quite well simulated (with very high correlation coefficients), and even some of the finer details of the observed seasonal cycle (e.g., the May minimum in wind speed at Lihue, Honolulu, and Kahului) are captured. The biases in the long-term mean seen earlier in Fig. 4 are apparent here in Fig. 5 as well, but the seasonal dependence of these biases is generally

modest. Perhaps the most notable systematic seasonal modulation of the model bias is in the SAT at Lihue, Honolulu, and Kahului, where there is a larger warm bias in summer than in winter.

The interannual fluctuations of the surface atmospheric fields are shown as time series from which the long-term mean seasonal cycle has been removed but in which the long-term annual mean is retained (Fig. 6). Specifically presented in Fig. 6 are 6-month running means of the deseasonalized SAT, wind speed, and rainfall at the four stations. These are compared with the HRCM-simulated values at the nearest land grid points. It is noteworthy that the year-to-year fluctuations in all fields at all stations appear to dominate any persistent linear trends, with the exception of surface wind speed at Hilo (discussed further below).

The correlation coefficients between these smoothed and deseasonalized SAT time series from HRCM simulation and observations are over 0.9 for all four stations, and the root-mean-square (RMS) differences between the
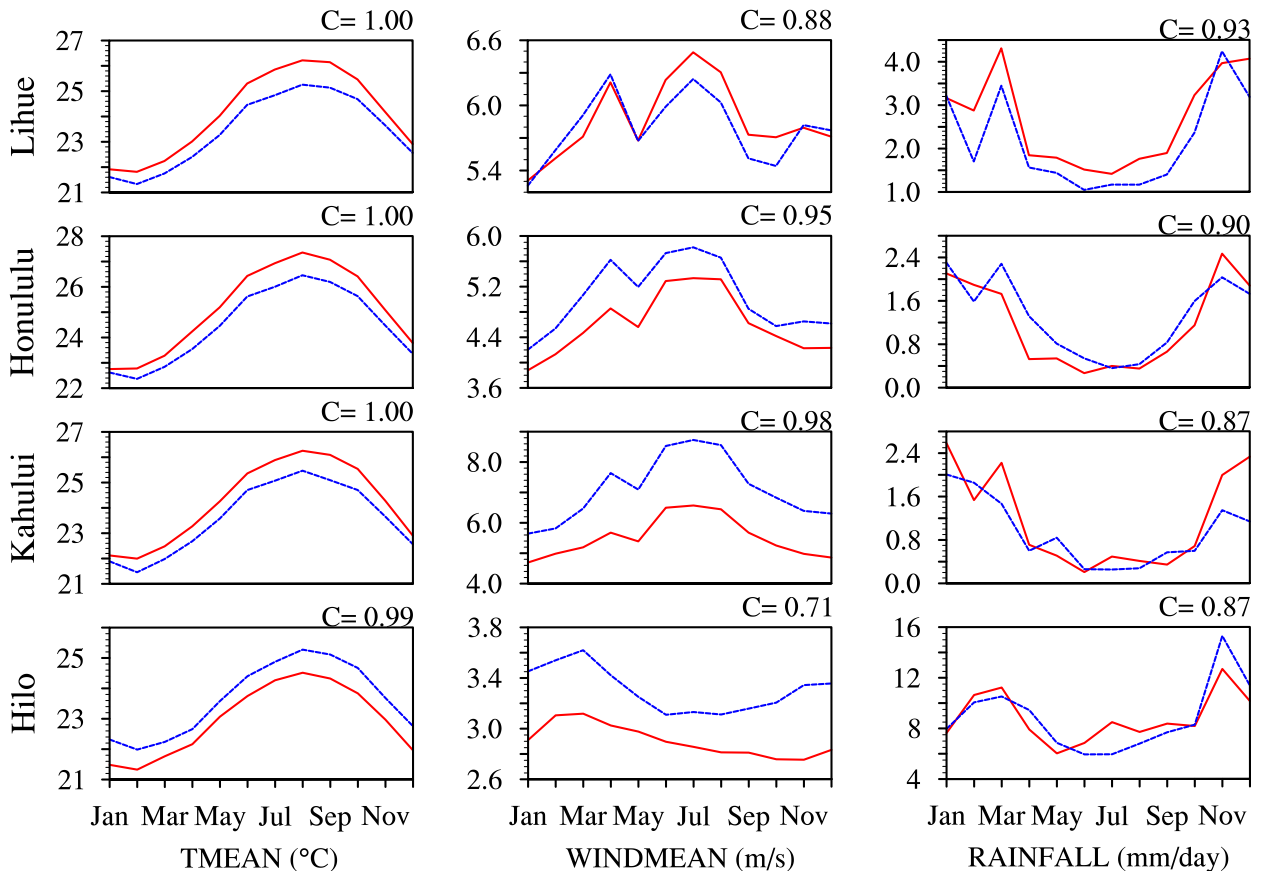
FIG. 5. (left)–(right) The 20-yr mean seasonal cycle for SAT, wind speed, and rainfall at (top)–(bottom) Lihue, Honolulu, Kahului, and Hilo, respectively. The red line is for station observations and the blue line is for the HRCM 3-km simulation at the nearest land grid points. The correlation coefficient *C* between the two curves is shown at the upper right corner of each panel.

series are less than 0.75°C. The HRCM-simulated interannual variations in wind speed appear to be reasonable at Lihue, Honolulu, and Kahului (with temporal correlation coefficients of 0.78–0.87), but the result at Hilo is quite anomalous. The observed record shows a strong trend over the 20-yr period of decreasing wind speed, which is completely absent in the model simulation. We do not have an explanation for this result and speculate that the cause may be inhomogeneity in the observed record, noting that the decrease in the observed wind speed takes place mainly in two steps around 1993 and 2002.

The right column of Fig. 6 compares the interannual fluctuations of rainfall simulated by the HRCM with the METAR station observations. Overall the model captures most of the largest fluctuations, notably the wet period around 1995–97 at Lihue, Honolulu, and Kahului and the very dry conditions around 1998–2000 at all four stations. At each station there are also some periods of 6–12 months of significant disagreement, particularly in the years since 2004. The correlation coefficients between the observed and modeled values range from 0.45 to 0.68.

b. Rainfall comparisons with gridded analyses: Geographical distribution

Figure 7 compares the 20-yr mean rainfall over the Hawaiian Islands in the simulation with that in the gridded observational data described in section 3 for the annual mean as well as the summer and winter halves of the year. Promisingly, the model captures all the main qualitative features seen in the complicated rainfall patterns on each of the islands. Specifically, one can identify in both observations and model simulation the following features: rainy windward slopes on all islands, the generally dry leeward rain shadow areas, the very wet summit on Kauai, and the two very dry summits on the Big Island (Mauna Kea and Mauna Loa). In both observations and model simulation the long-term mean daily rainfall exceeds 20 mm at some points on the windward sides of east Maui and the Big Island. The spatial correlation coefficient between the gridded observations and model simulation of long-term mean rainfall evaluated on the 3-km grid over all the land areas in Hawaii was 0.83 for the annual mean and 0.84 and 0.79 for
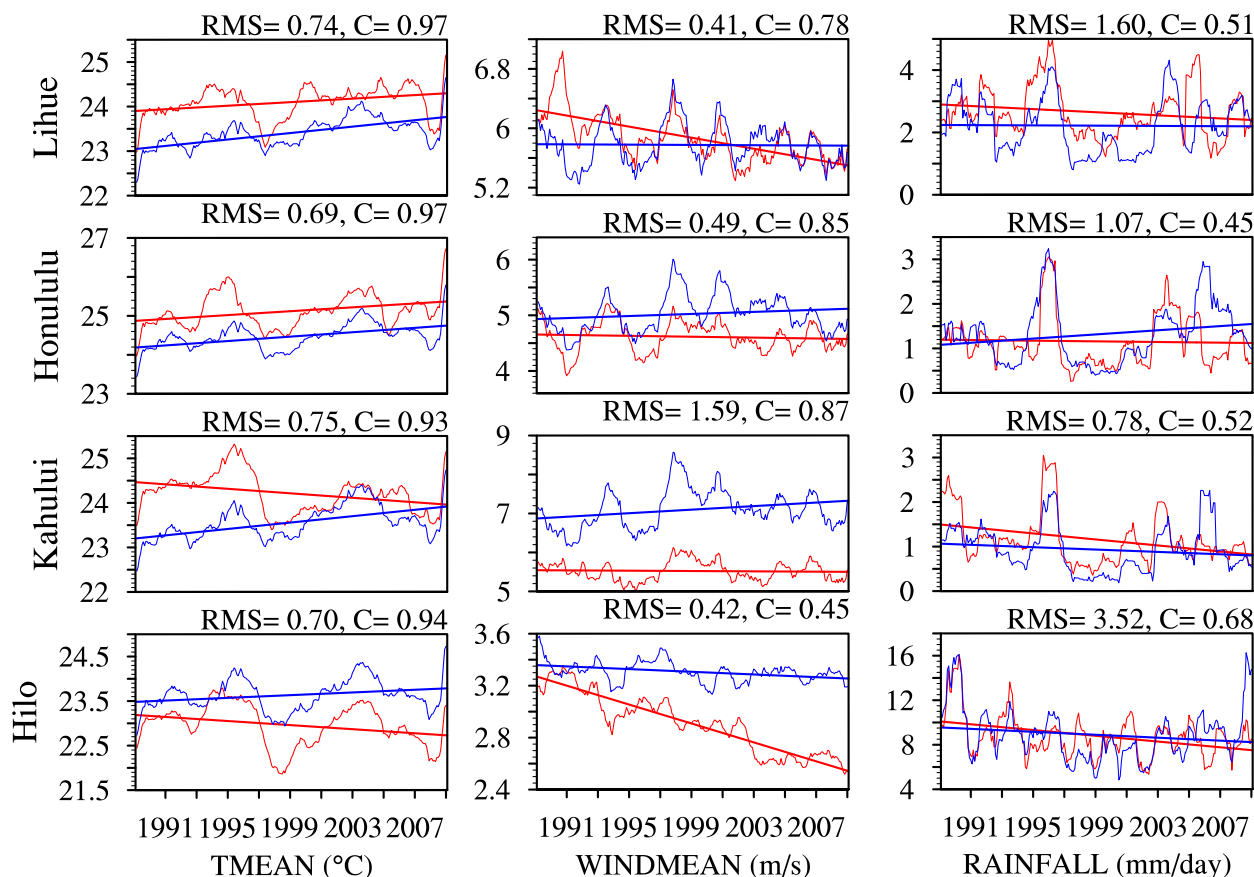
FIG. 6. (left)–(right) The time series of mean SAT, wind speed, and rainfall at (top)–(bottom) Lihue, Honolulu, Kahului, and Hilo. Quantities shown are 6-month running means. Red curves are for the station observations, and blue is for the HRCM 3-km simulation at the land grid point nearest to the station. The mean RMS difference between model and observational curves and the correlation coefficient *C* between the two curves are shown. The least squares linear regression trends over the 20 yr are also shown as straight lines in each panel.

winter and summer, respectively. The 20-yr annual-mean rainfall rate for the land areas of all the Hawaiian Islands is 4.54 mm day^{-1} in the gridded observations and slightly lower (4.49 mm day^{-1}) in the HRCM simulation. Compared with the observational analysis, the model mean rainfall over land areas has an overall wet bias of 6% in winter and a dry bias of 12% in summer.

While the pattern of overall geographical variation in the climatological rainfall looks reasonable in the model, many particular details are not very well simulated. Some of the most obvious problems occur over Oahu and Maui. The rainfall maximum along the mountains stretching along the east coast of Oahu is too weak in the model. On west Maui the HRCM reproduces the rainfall maximum near the topographic summit, but the rainfall rate there is underestimated by ~5 mm day^{-1} (i.e., by ~40% of the mean observed value). The observed mean rainfall on east Maui has a maximum along the topographic slopes facing northeastward, and the area around the summit of

Mt. Haleakala is quite dry. In the model simulation the rainfall maximum on east Maui is concentrated on the east end, and the southeast–northwest-oriented rain maximum along the northeast facing slope in the observations is absent. The heavy rainfall region in the model also penetrates rather close to the mountain summit. These deficiencies over Oahu and Maui have a clear signature in the bias maps (Figs. 7c,f,i), and the pattern of the biases over those islands is similar in winter and summer. The major topographic features on both Oahu and Maui exhibit steep slopes and small horizontal scales. The mountains along the east coast of Oahu are particularly narrow and are significantly smoothed and biased low in the 3-km representation. Given that most of the rainfall here is due to topographic interaction with the atmospheric low-level flow, it is not surprising that the model underestimates rainfall along the mountain range. On Maui, as well, the topographic slopes on the mountains in both east Maui (Mt. Haleakala) and west Maui are
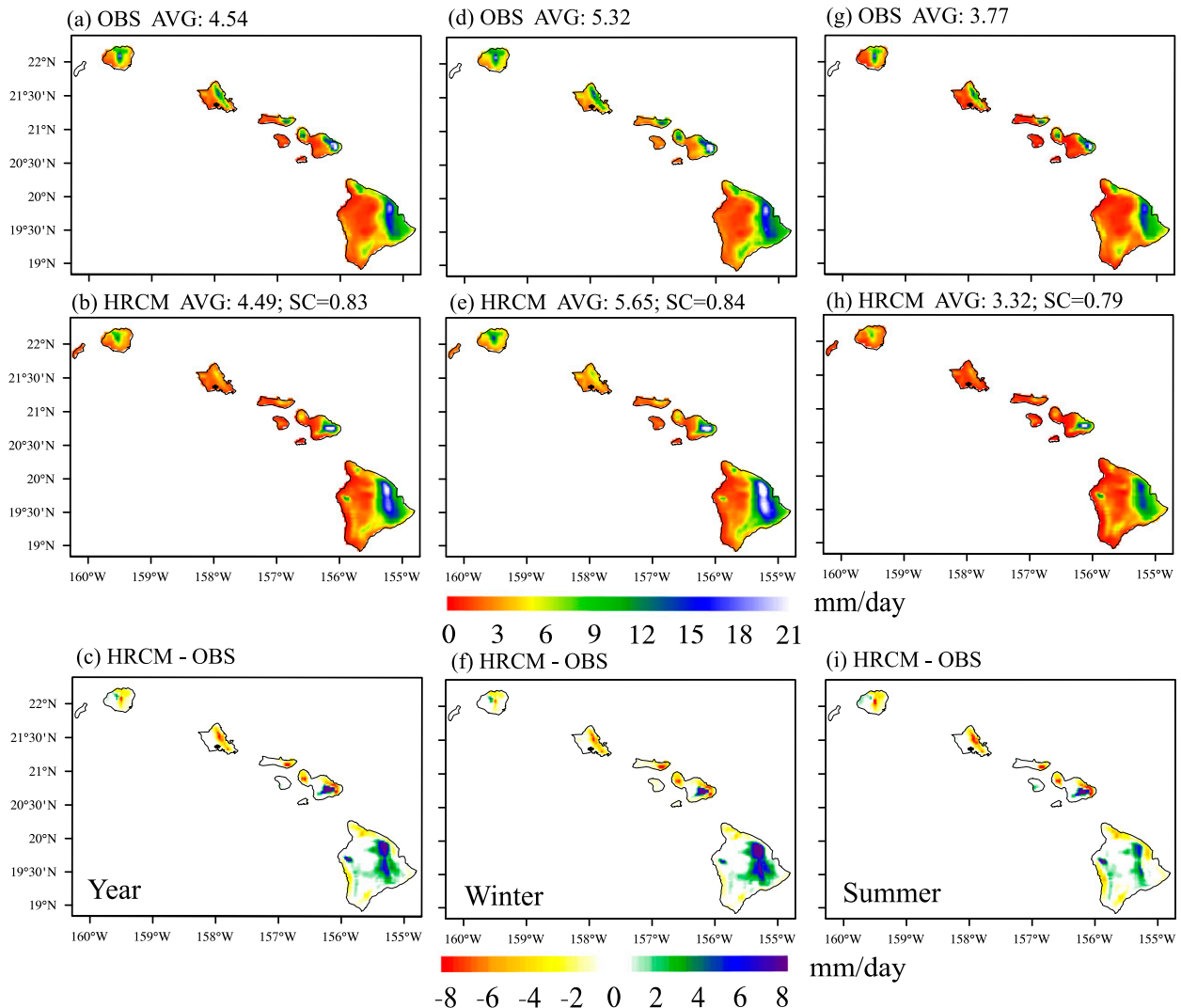
FIG. 7. (a) The observed 20-yr annual-mean rainfall based on several hundred measurement stations (see text for details). (b) The simulated annual-mean rainfall from the 3-km HRCM simulation. The SC over the land is calculated for 3-km grids. Also shown at the top of the panel is the average rainfall amounts (mm day^{-1}) over all land areas. (c) The model bias (model − observations). The winter (d) observations, (e) model results, and (f) model biases. (g)–(i) As in (d)–(f), but for summer.

large, and the 3-km version of the Maui orography is also considerably smoothed. We have addressed this issue explicitly for Maui with our 1-km "innermost domain" simulation, which we will discuss in section 6 below.

On the Big Island the pattern of wet and dry areas is well captured in the model simulation. The model produces a long, narrow maximum in mean rainfall along the west coast of the Big Island corresponding to that observed but centered slightly more inland (Figs. 7b,e,h). The biggest bias in the simulated mean rainfall on the Big Island evident in Fig. 7 is an over-estimation of rainfall along the main topographic slope on the east part of the island, particularly in winter. In winter this bias is as high as ~8 mm day^{-1}, representing

a ~40% overestimation of local rainfall. The topography on the Big Island is smoother than on the other major Hawaiian Islands, so, in contrast to the case for Oahu and Maui, we expect that the resolution of the topography in the 3-km domain is not a major factor in the model bias; however, the advection scheme for water vapor might play an important role, which will be a topic for a future work.

Overall we regard the mean rainfall simulation as successful, but there are model biases at many individual locations that are as much as ~(30%–40%) relative to the Hawaiian rainfall observations and at some exceptional locations, such as the summit of Mt. Haleakala on Maui, can be even larger.
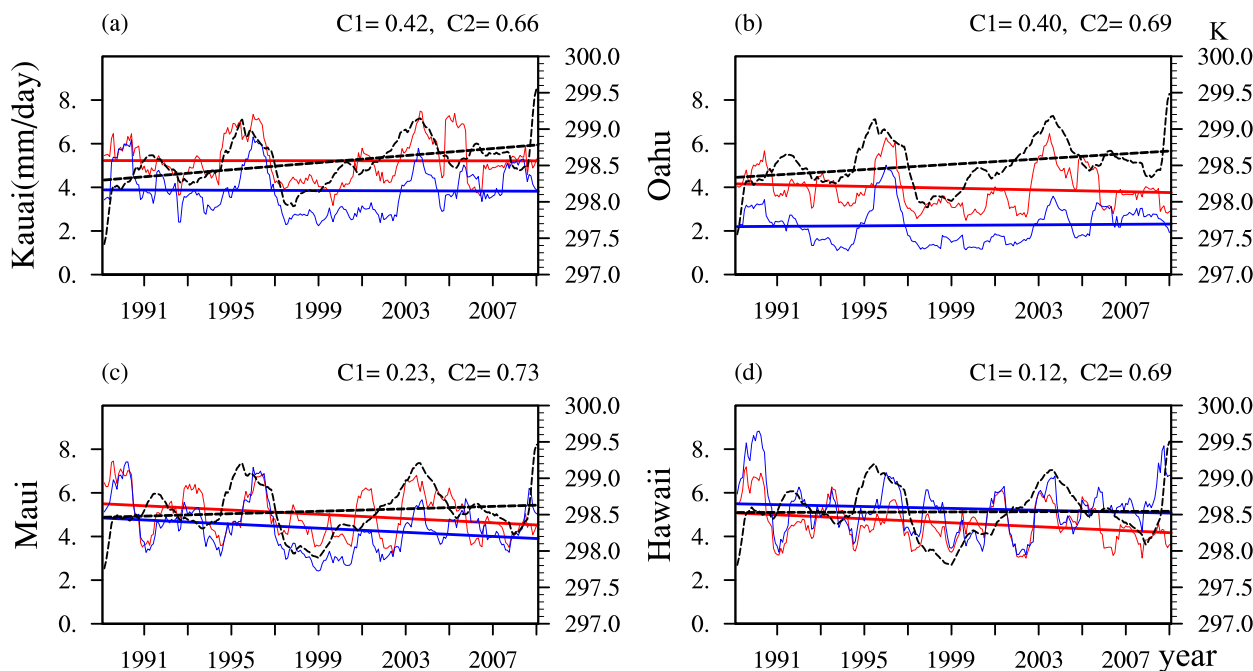
FIG. 8. The interannual variations of the rainfall (red is for observations; blue is for the HRCM 3-km simulation) and local SST (black) for Kauai, Oahu, Maui, and Hawaii. The C1 and C2 denote the correlation coefficient between local SST and observed rainfall and between observed and simulated rainfall, respectively. The trends are also shown in the figure as straight lines.

c. Rainfall comparisons with gridded analyses: Interannual variations

Figure 8 presents the individual island mean rainfall values shown as time series from which the long-term mean seasonal cycle has been removed but with the long-term annual mean retained, as in Fig. 6. Results shown have been smoothed with a 6-month running mean, and values for the observations and the HRCM simulation are compared. Just as we saw for individual station rainfall observations (Fig. 6), the linear trends are small relative to the other year-to-year variations apparent. The model simulation reproduces the main wet and dry periods seen in the observations. Overall the agreement between the model simulation and observations appears much better for these island averages (correlation coefficients of 0.66–0.73) than for the individual station values in Fig. 6 (correlation coefficients of 0.45–0.68).

Also shown by the black curves in Fig. 8 are estimates of the "local SST" around each island [average of the Reynolds et al. (2010) satellite SST analyses over a 2.5° × 2.5° box centered on each of Kauai, Oahu, and Maui and over a 4° × 4° box around the Big Island; a map of the 20-yr trend in observed SSTs is shown in the appendix]. The local SST appears to have a modest positive correlation with the rainfall over Kauai and Oahu. However, the correlation between SST and island mean rainfall is very weak for Maui and the Big Island. In general the SST changes are

slower than the high-frequency variations in rainfall evident even in the 6-month smoothed curves in Fig. 8.

d. Diurnal rainfall variation

The average rainfall in Hawaii exhibits significant diurnal variations, which have been documented in many earlier observational studies (e.g., Schroeder et al. 1977; Chen and Nash 1994; Sen Roy and Balling 2004; Hartley and Chen 2010). The diurnal variations themselves have a complicated geographical dependence presumably related to the topography on each island. As noted in section 3b, we have interpolated the hourly rainfall observations archived at NCEI and at Hydronet stations for 1995–2009 onto the 3-km grid, from which 15-yr mean statistics were computed. Figure 9a presents maps of the local time at which the diurnal cycle of mean rainfall amount peaks. Figure 9c shows the same quantity for the diurnal cycle of rainfall frequency. Figures 9b,d present comparable values computed from the same 15 years of the HRCM simulation. Note that the observations are plotted only over land, while we show model results also over adjacent ocean regions. The peak time is calculated by fitting a 24-h sine wave to the long-term means calculated for each hour of the day. The results for mean rainfall peak and maximum frequency of rainfall are rather similar (cf. Figs. 9a and 9c or Figs. 9b and 9d). Within each major island there are very significant geographical variations in the phase of
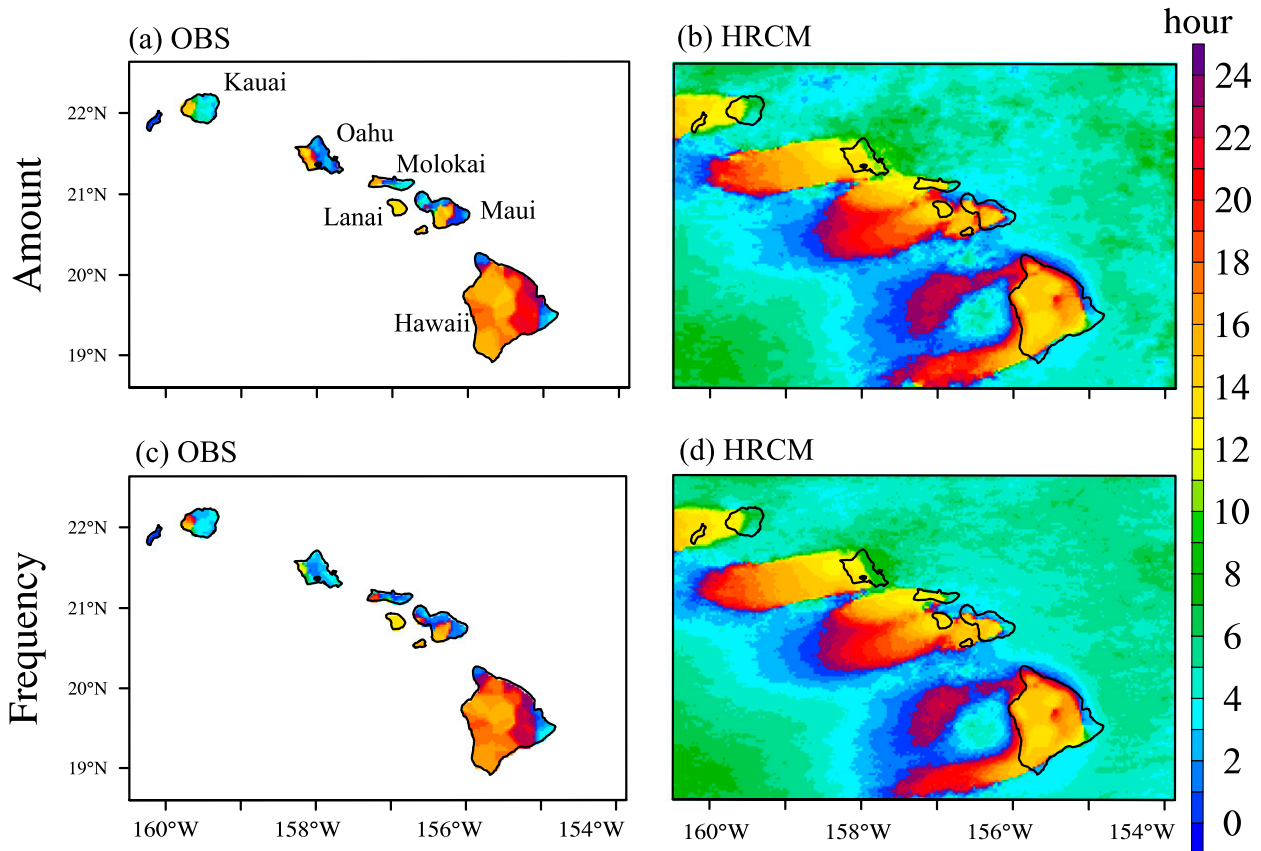
FIG. 9. Phase of the diurnal harmonic of long-term-mean–annual-mean rainfall. Specifically shown are the LT peak of the diurnal (24 h) harmonic of the (a),(b) mean rainfall rate and (c),(d) rainfall frequency: (a),(c) gridded observations over land and (b),(d) the HRCM simulation.

the diurnal cycle. There is an overall pattern of early morning peaks [0200–0600 local time (LT)] over the windward sides and afternoon peaks (1200–1500 LT) on the leeward sides. This pattern is evident on east Maui, Oahu, and Kauai, and even on the rather small island of Molokai. The diurnal rainfall cycle on the Big Island displays even more intricate geographical dependence with a transition from early morning (0200–0400 LT) at the extreme eastern end to late evening (1800–2200 LT) in a substantial band over much of the eastern third of the island. Most of the western two-thirds of the island has mid-to-late afternoon peaks (1400–1800 LT) with a region of near-midnight peaks on the northern tip of the island.

The HRCM simulation also shows large variations in diurnal phase within each island. The overall agreement of the simulated patterns with observations is reasonably good, although the model simulation and observations differ in many details. The most notable biases in the HRCM simulation are on the windward sides of Oahu and Kauai where the amount and frequency peaks are around 3 h later than indicated in the rain gauge

observations. Estimates of the amplitude of the climatological diurnal cycle in rainfall (not shown) are also fairly similar in the observational analysis and in the HRCM simulation.

e. Trade wind inversion climatology

The red curves in Figs. 10c,d show the 20-yr time series of monthly means of the TWIBH at Lihue and Hilo computed from the twice-daily balloon soundings at each station. These monthly averages are computed only using soundings with a well-defined TWI. Details of the definition of TWI and TWIBH we employed are given in Zhang et al. (2012b). The same definitions were used to determine the mean TWIBH in the HRCM simulation, and Figs. 10c,d compare the observed (balloon radiosonde) TWIBH and that from the HRCM simulation at the grid points nearest to Lihue and Hilo. The annual and interannual variations in the TWIBH at both stations are simulated reasonably well (with correlation coefficients of 0.71 and 0.74), but the model has a rather persistent low bias of ~100 m.
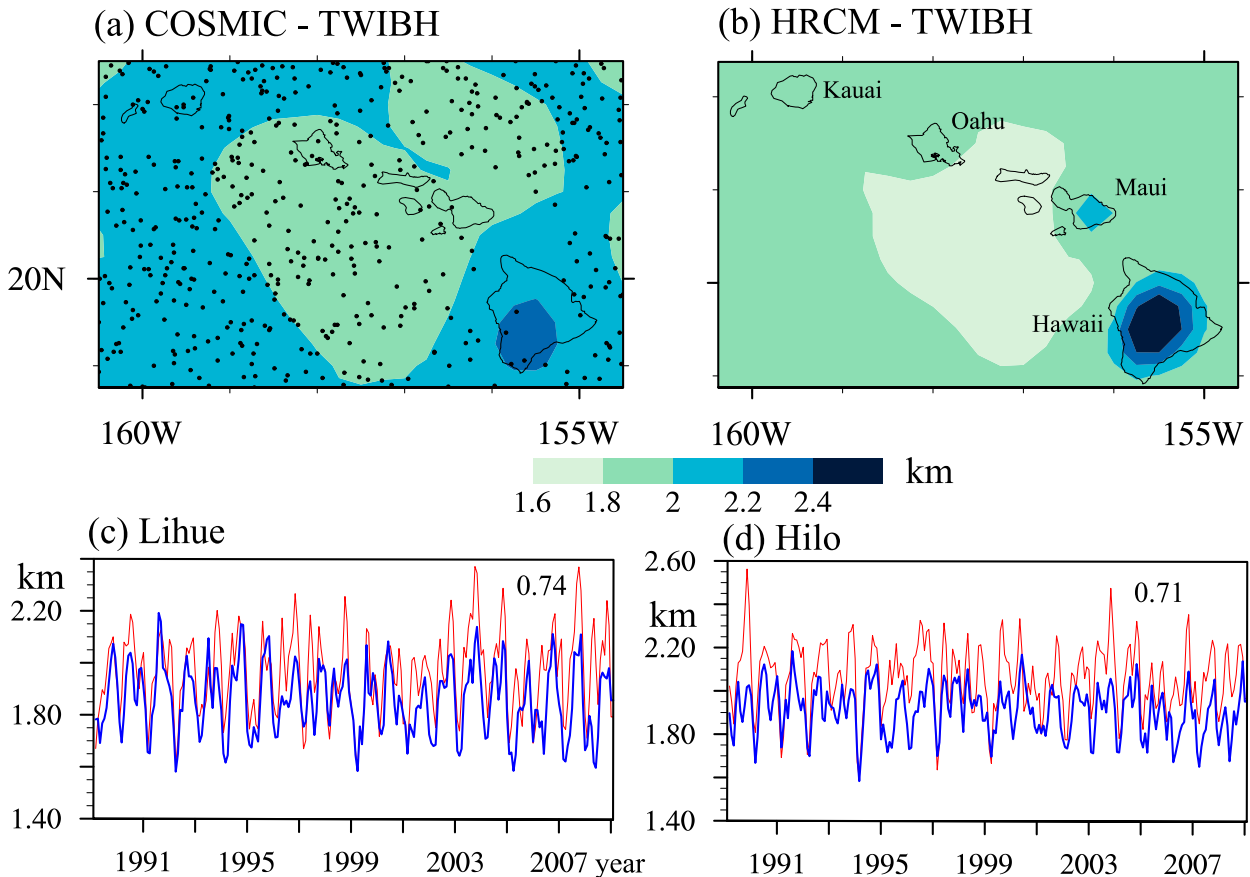
(a) COSMIC - TWIBH

(b) HRCM - TWIBH

FIG. 10. The TWIBH derived from the (a) COSMIC observations and the (b) HRCM simulation. The black dots in (a) are the locations of the observed profiles from COSMIC. The time series of monthly mean of the TWIBH computed from balloon soundings at (c) Lihue and (d) Hilo are shown by the red curves. The values from the HRCM simulation are shown by the blue curves. The correlation coefficient between the observed and modeled time series is shown in the upper right corner of each panel.

As discussed earlier in section 3, Zhang et al. (2012b) also estimated TWIBH from satellite radio occultation measurements, which provide the opportunity to evaluate the geographical variations of TWIBH in the model simulation. Figure 10a shows our estimated TWIBH based on these satellite radio occultation observations. This exercise is limited by the relatively few soundings available (see Fig. 10a) and the limited period (2006–10) covered. The contour map is drawn using an interpolation that lumped together all the data over this period and can be regarded as an estimate of the long-term annual-mean TWIBH (see Zhang et al. 2012b). A comparable long-term mean TWIBH was also computed from the HRCM simulation (Fig. 10b). Note that the model results have been smoothed horizontally to ~25-km resolution to make them somewhat comparable to the observations in equivalent resolution. This explains why the model mean TWIBH shown is only about 2–2.5 km above sea level in areas on the Big Island and Maui where topographic heights are actually higher.

The overall low bias of ~100 m noted earlier in the model TWIBH is evident, but the model simulation does capture the overall geographical structure of the TWI around Hawaii that is apparent in observations. Notably the TWIBH is highest near the major islands and is lower on either side, especially in a "bowl" of radius ~100 km, centered near 20°N, 157°W (i.e., southwest of Oahu and Maui and west of the Big Island).

f. Comparisons with SAT station data

The fact that the HRCM is able to simulate SAT at the METAR stations with biases less than 1°C (Figs. 4–6) may not be surprising, given that the stations are all near the coast and observed SSTs are prescribed in the model simulation. Here we evaluate the HRCM simulation using the larger database of SAT observations from 44 stations (mainly NOAA cooperative stations) described in section 3b. This network of stations is shown in Fig. 11a and includes several inland and high-altitude locations.
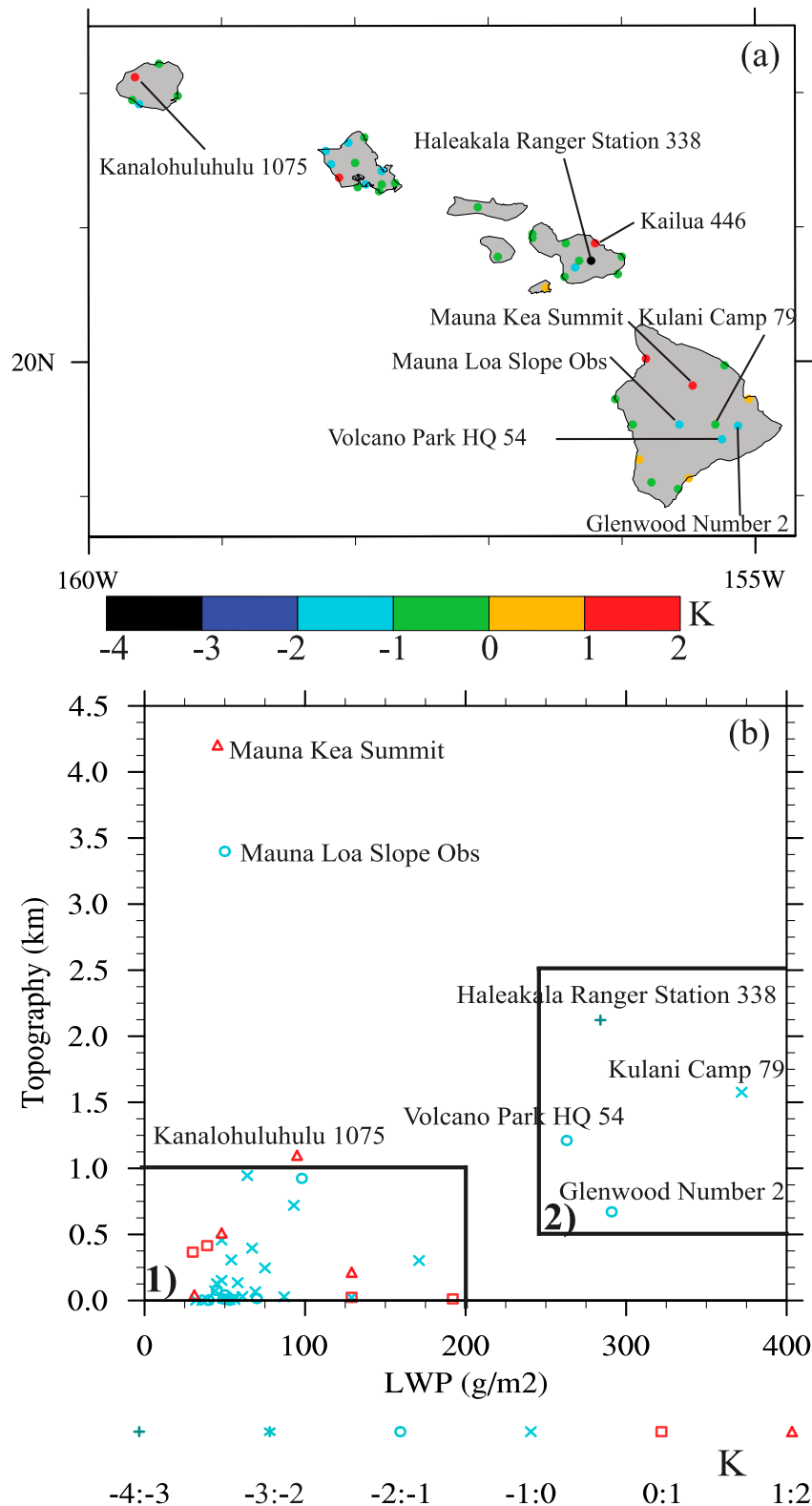
FIG. 11. (a) The distribution for the 20-yr mean SAT (K) bias (HRCM simulations −
observations) over the Hawaiian Islands. (b) The temperature biases for each station related to
LWP and topography are also shown with "1)" including the low topography stations and "2)" the
stations in the cloud zone in the model. Some station names are also marked in the panels.

Figure 11a presents the 20-yr mean bias of the model-simulated SAT relative to each station's observations. To produce this comparison, we interpolated the HRCM grid values onto the exact station locations by a bilinear interpolation method. The SAT biases over low terrain areas are typically less than 1°C (box 1 in Fig. 11b). However, the biases are larger (1°–3°C) over high-elevation areas (Fig. 11b). We then computed a correction based on the differences in elevation between the interpolated model topography and the actual height above sea level at the station locations. The differences in elevation at most stations are less than 100 m, and the largest bias is at the Mauna Kea summit (elevation 4205 m), where the terrain height in the model is about 350 m lower than the actual terrain height (Table 1). The simulated SAT can be adjusted to the real station height by assuming a lapse rate of 6.5°C km^{-1} (Table 1). After applying this correction, the SAT bias at the summit of Mauna Kea goes down from 1.7° to −0.5°C. Overall 50% of 44 stations show a smaller SAT bias after this correction, while 34% of the stations have larger SAT biases. At some stations in box 2 of Fig. 11b (e.g., Kulani camp 79, volcano park HQ 54, and Glenwood number 2), the negative SAT biases are larger after the elevation correction as a result of the lower model topography height compared to the real height. There is still a 2.2°C bias at Haleakala ranger station 338 after applying a 1.1°C adjustment. Figure 11b shows liquid water path (LWP) versus elevation for the surface stations investigated here. Since clouds in Hawaii are typically low clouds (cloud tops below 2.5 km) there is often no ice or mixed phase. The LWP is therefore closely related to the cloud amount and is used here in combination with the elevation of a station to determine whether the station is in the cloud zone in the model (box 2 in Fig. 11b) or not (box 1). To explain why all four windward cloud zone stations have relatively large negative SAT biases, we compared the simulated 20-yr net radiation climatology to the retrieved net radiation at the surface by Giambelluca et al. (2014) for the Hawaiian Islands (Fig. 12). The retrieved net radiation is between 80 and 120 W m^{-2}, while the simulated net radiation is between 50 and 110 W m^{-2} over the windward sides of the Big Island and Maui (Figs. 12a,b). The total cloud fraction (TCF) and liquid water path are both important factors controlling the net radiation at the surface. There is a slightly higher TCF in the model simulation compared with the TCF retrieved from satellite observations over the windward sides of the islands of Hawaii and Maui (Figs. 12c,d). The overestimated TCF is likely contributing to the negative bias of the net surface radiation in the model. Unfortunately, there are no high-resolution LWP observations over Hawaii to evaluate the modeled LWP.

6. Innermost domain (1 km) simulation over Maui

As noted above it seems plausible to attribute much of the deficiencies in the mean rainfall simulation over Oahu and Maui in our intermediate (3 km) domain to the overly smoothed representation of the topography on these islands. We therefore included a 1-km-resolution nested innermost domain around Maui in our simulation (Fig. 1). The observed long-term mean rainfall on Maui (Fig. 13a) shows a very uneven distribution and sharp horizontal gradients. Mean rainfall exceeds 20 mm day^{-1} at some places on the windward side of Mt. Haleakala in east Maui and near the summit of the mountains in west Maui but is an order of magnitude less over much of the central parts of the island. The sharp gradients presumably result from interactions of the low-level wind with the Maui's steep topography.

Figure 13c shows the 20-yr annual-mean rainfall from the intermediate domain (3 km) simulation (i.e., just a detail from Fig. 7b). The deficiencies noted earlier in section 5 are apparent, notably the rainfall maximum on the eastern side of east Maui is oriented east–west in the simulation rather than southwest–northwest as in the observations. The high rainfall axis penetrates too close to the summit of Mt. Haleakala (elevation 3055 m), which in observations is quite dry. The numbers on Fig. 13a show the locations of NCEI stations from which rainfall data are available (note that this is only a fraction of all rainfall stations used to create the gridded dataset used to produce Fig. 13a). Table 2 shows the observed long-term mean rainfall rate at each station and the simulated values in the 3- and 1-km domains of the HRCM. On west Maui the model correctly simulates a rainfall maximum near the highest topography, but the peak rainfall there is underpredicted by ~50%.

Figure 13b shows the simulated mean rainfall rates in the 1-km-resolution domain simulation. The great improvement in the pattern of rainfall compared with the simulation in the 3-km-resolution domain is evident. The results for the individual NCEI stations in Table 2 are almost all improved substantially in the 1-km simulation. Notably at station 1 the bias of more than 300% in the 3-km simulation is reduced to 33% in the 1-km-resolution simulation.

7. Discussion and conclusions

We integrated a triply nested version of the HRCM for 20 yr that was forced by global reanalysis data and observed SSTs. The horizontal resolution is 15 km over an extensive ocean area in the central equatorial and North Pacific, 3 km for the Hawaiian Islands and adjacent
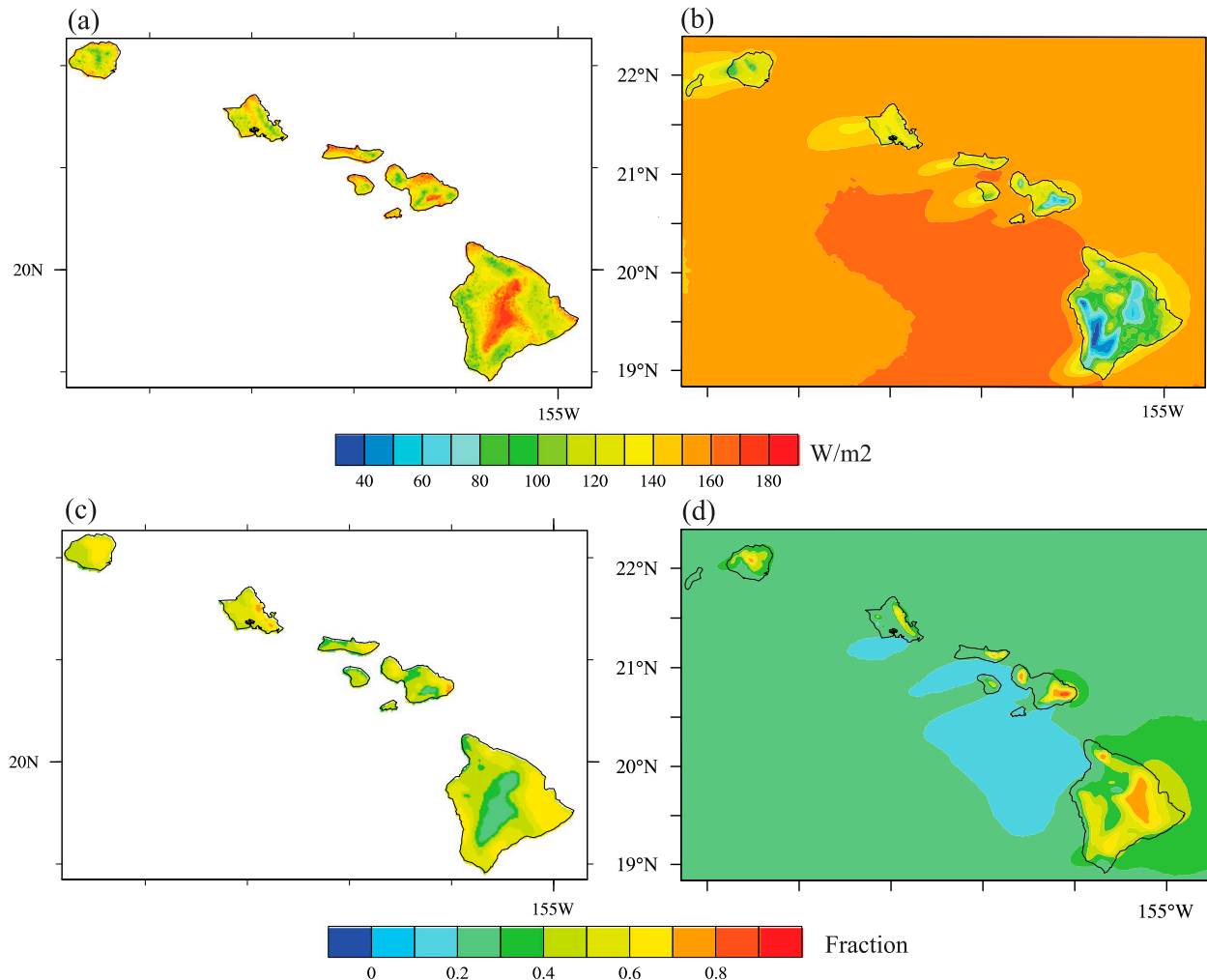
FIG. 12. (a) The retrieved net radiation at the surface, (c) total cloud fraction climatology by Giambelluca et al. (2014), (b) the model-simulated climatology of net surface radiation, and (d) total cloud fraction.

oceans, and 1 km for the island of Maui and surroundings. The basic features of the regional-scale climatology simulated in the HRCM outermost domain, including the mean location of the ITCZ and long-term mean SLP patterns, are reasonably well reproduced by the model.

The intermediate 3-km-resolution domain results were compared with a wide variety of local station and other high-resolution observations in order to evaluate how well the HRCM can simulate the fine structure of Hawaiian microclimates. Near the coasts, the model long-term mean SAT biases relative to station observations are almost everywhere less than 1°C—agreement that presumably is largely ordained by the prescription of observed SSTs in the adjacent ocean regions. At inland locations the model-simulated SAT is less directly constrained by the SSTs, and model biases in SAT in the 1°–2°C range are common at many

locations, with the bias exceeding 3°C at one station (Fig. 11). The simulated long-term mean rainfall was compared with observations at some individual stations and with a gridded analysis over all land areas derived from a sophisticated optimal interpolation of several hundred station observations. The overall geographical and seasonal patterns of rainfall over the islands are captured reasonably well in the HRCM simulation. The spatial correlation coefficient between interpolated observations and model simulation of long-term mean rainfall evaluated on 3-km grids over all the land areas in Hawaii was 0.79–0.84 depending on the season considered. However, we find model biases at individual locations that are ∼(30%–40%) relative to the interpolated observations. Overall, the HRCM biases in simulated climatological SAT and rainfall at individual locations over the Hawaiian Islands seem fairly modest.
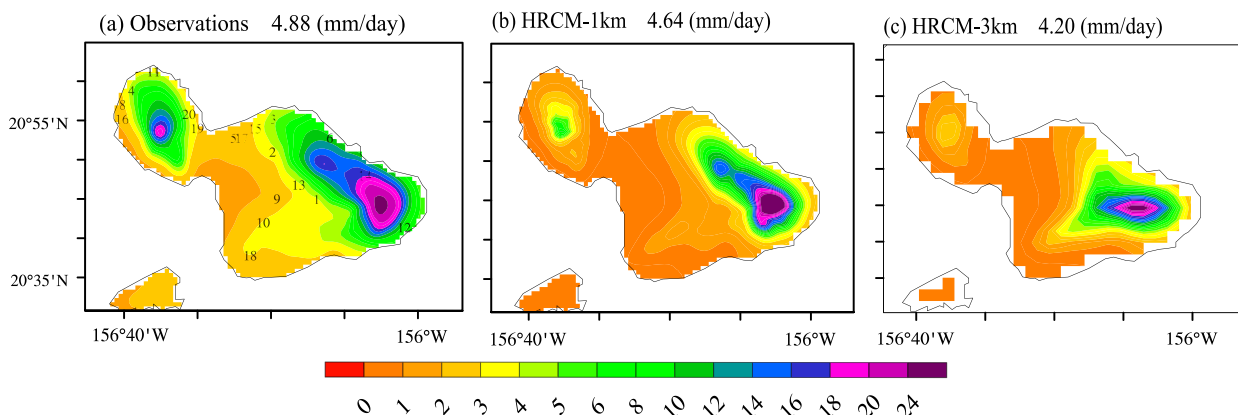
FIG. 13. The 20-yr mean rainfall in (a) observations, (b) the HRCM 1-km simulation, and (c) the HRCM 3-km simulation. The numbers in (a) are the NCEI observational stations listed in Table 2.

More detailed analysis of rain gauge data and model output showed that the HRCM simulates a quite realistic diurnal cycle of rainfall. This result is gratifying as this aspect of the circulation is generated internally within the model and is not strongly controlled by the prescribed boundary conditions.

We used objective criteria to classify any observed or simulated atmospheric sounding as representing typical TWI conditions or not and found a TWI frequency of about 80% in both observations and the model simulation. The TWI periods of the record were analyzed to create the climatology of TWI height in the model, which

was compared to TWI statistics from balloon soundings and GPS satellite profiles. While there is basic agreement in the geographical and seasonal variations of the mean TWI in the observations and model simulation, the HRCM does display a fairly consistent low bias of ~100 m in the TWIBH.

We also analyzed aspects of the interannual variations in the simulated rainfall, SAT, and surface wind speed. The overall strength of interannual fluctuations in rainfall is reasonably well captured in the simulations. The detailed time series of the modeled rainfall, SAT, and surface wind speed over the 20-yr period are

TABLE 2. The NCEI rainfall stations (location of each station is shown in Fig. 13a) over Maui with the observed and HRCM-simulated long-term mean rainfall rates. The rainfall biases are highlighted in italic, and the rainfall biases of percentage are highlighted in boldface.

| Station	Latitude (°N)	Longitude (°E)	Elevation (m)	Obs (mm day^{-1})	3-km simulation			1-km simulation		
					Mean (mm day^{-1})	Bias (mm day^{-1})	Bias (%)	Mean (mm day^{-1})	Bias (mm day^{-1})	Bias (%)
1	20.75	−156.23	2122	3.2	14.9	*11.8*	**369**	4.2	*1.1*	**33**
2	20.85	−156.33	329	3.0	2.0	*−1.0*	**−34**	2.7	*−0.3*	**−10**
3	20.92	−156.33	98	3.0	2.1	*−0.9*	**−29**	3.1	*0.1*	**2**
4	20.98	−156.65	67	2.4	1.6	*−0.8*	**−34**	2.8	*0.4*	**17**
5	20.88	−156.42	16	1.1	0.9	*−0.2*	**−18**	1.1	*−0.0*	**−4**
6	20.88	−156.20	213	8.3	5.8	*−2.5*	**−30**	7.6	*−0.7*	**−8**
7	21.18	−156.97	9	2.9	2.0	*−0.9*	**−32**	2.1	*−0.8*	**−26**
8	20.95	−156.67	73	1.9	1.1	*−0.8*	**−41**	1.8	*−0.1*	**−6**
9	20.75	−156.32	945	1.5	2.2	*0.7*	**43**	1.6	*0.1*	**4**
10	20.70	−156.35	924	2.0	3.2	*1.2*	**58**	1.6	*−0.4*	**−18**
11	21.02	−156.60	107	2.6	1.8	*−0.8*	**−32**	2.1	*−0.5*	**−21**
12	20.69	−156.03	28	5.7	5.2	*−0.5*	**−9**	6.4	*0.6*	**11**
13	20.78	−156.27	1256	3.7	6.3	*2.6*	**69**	2.9	*−0.9*	**−23**
14	20.80	−156.12	383	13.6	8.0	*−5.6*	**−41**	14.1	*0.6*	**4**
15	20.90	−156.37	52	2.0	1.3	*−0.6*	**−32**	1.9	*−0.1*	**−5**
16	20.92	−156.67	128	1.7	1.1	*−0.6*	**−36**	1.3	*−0.4*	**−25**
17	20.88	−156.40	27	1.5	1.0	*−0.5*	**−32**	1.3	*−0.2*	**−14**
18	20.63	−156.38	579	2.1	1.3	*−0.8*	**−38**	1.6	*−0.4*	**−20**
19	20.90	−156.50	98	2.2	1.1	*−1.1*	**−51**	1.3	*−1.0*	**−43**
20	20.93	−156.52	104	2.9	1.6	*−1.4*	**−47**	1.8	*−1.1*	**−38**
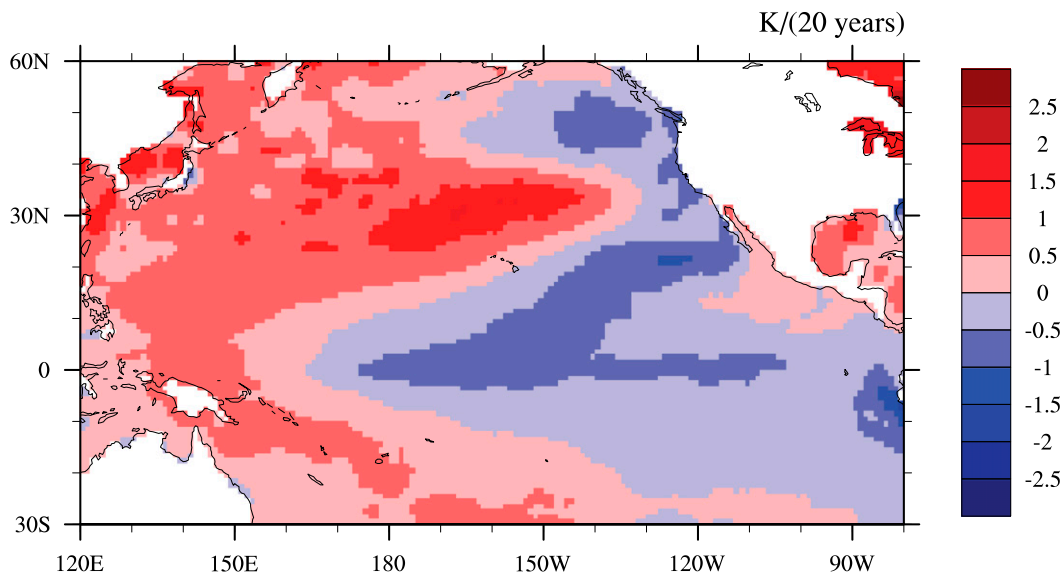
FIG. A1. The trend in the Reynolds et al. (2010) observed SSTs $[K (20 yr)^{-1}]$ over the time period 1990–2009 based on a linear regression of the monthly mean values at each grid point.

reasonably close to observations (Figs. 6 and 8). The most striking feature of the observed rainfall records—namely, the heavy rain in 1995/96 followed by a protracted period of below-average rainfall until 2001—is reproduced to some extent in the HRCM simulation. The observed time series over the period showed significant variability on a range of time scales, and in none of the records did consistent long-term trends appear to be the dominant contribution to interannual variability. Nonetheless we did examine the 20-yr linear trends in the observed and simulated SAT and rainfall fields and found some degree of agreement. Any 20-yr trends in regional atmospheric conditions would be forced primarily by the 20-yr trends in SST in the Pacific basin, and those SST trends are up to $\sim 0.1°C yr^{-1}$ locally and have substantial geographical structure. These 20-yr SST trends are likely dominated by just sampling of low-frequency natural variability such as the Pacific decadal oscillation (PDO) and have little resemblance to the SST warming patterns anticipated over longer time scales from anthropogenic climate forcing.

Ideally we would like to show that the statistical properties of the HRCM simulation (such as long-term mean rainfall rates) have converged at the grid resolution employed. As for most comprehensive climate simulations we do not have the luxury of demonstrating numerical convergence of our solutions or of being able to confidently say how much any remaining deficiencies in the simulations can be ascribed to the finite grid resolution of the model. However, on the Big Island the relatively smooth geographical patterns in both observed and modeled mean rainfall suggest that the 3-km horizontal grid spacing in our intermediate domain may be adequate. But the topography on each of Maui, Oahu, and Kauai is overall steeper than on the Big Island and aspects of the topography seem not adequately resolved even in 3-km grids. As part of this study we included an innermost domain with 1-km horizontal resolution over the island of Maui. The results in the 1-km simulation showed substantial improvement of the simulated mean rainfall climatology. This improvement can be plausibly explained by the better resolution of the topography on the 1-km grids. Our planned future work includes exploring simulations with enhanced-resolution model grids over Oahu and Kauai.

Despite some remaining biases, the overall success of the HRCM in reproducing Hawaiian microclimate over the 20-yr historical period considered here gives us confidence that the model is suitable for application to fine-spatial-resolution climate change projections for the Hawaiian Islands. Part II of this work will present the results from HRCM simulations designed as a projection for global climate conditions of the late twenty-first century. Results of the simulations reported in this two-part paper will be publicly available at the Asia-Pacific Data-Research Center of the University of Hawai'i at Mānoa (http://apdrc.soest.hawaii.edu/).

APPENDIX

Low-Frequency SST Variability

The observed and modeled rainfall time series shown in Figs. 6 and 8 reveal significant variability from year to year as well as at decadal and possibly even longer time scales. Measures of observed statewide rainfall show correlations with the phase of the Pacific decadal oscillation (PDO; e.g., Chu and Chen 2005), and it is reasonable to suppose that the changes in Hawaii rainfall on long time scales are largely driven by the regional- to basin-scale SST variations associated with the PDO. There may also be a consistent warming trend in the SST variations that represent the effects of anthropogenically forced global warming. The actual trend in the SST (Fig. A1) over our period of interest has little resemblance to the SST warming pattern anticipated over longer time scales from anthropogenic climate forcing and is probably best regarded as resulting primarily from the 20-yr sample of low-frequency natural variability such as the PDO.

REFERENCES

Adler, R. F., and Coauthors, 2003: The Version-2 Global Precipitation Climatology Project (GPCP) monthly precipitation analysis (1979–present). *J. Hydrometeor.*, **4**, 1147–1167, doi:10.1175/1525-7541(2003)004<1147:TVGPCP>2.0.CO;2.

Alexandru, A., R. de Elia, R. Laprise, L. Separovic, and S. Biner, 2009: Sensitivity study of regional climate model simulations to large-scale nudging parameters. *Mon. Wea. Rev.*, **137**, 1666–1685, doi:10.1175/2008MWR2620.1.

Bowden, J. H., T. L. Otte, C. G. Nolte, and M. J. Otte, 2012: Examining interior grid nudging techniques using two-way nesting in the WRF Model for regional climate modeling. *J. Climate*, **25**, 2805–2823, doi:10.1175/JCLI-D-11-00167.1.

Cao, G., T. W. Giambelluca, D. E. Stevens, and T. A. Schroeder, 2007: Inversion variability in the Hawaiian trade wind regime. *J. Climate*, **20**, 1145–1160, doi:10.1175/JCLI4033.1.

Castro, C. L., R. A. Pielke Sr., and G. Leoncini, 2005: Dynamical downscaling: Assessment of value retained and added using the Regional Atmospheric Modeling System (RAMS). *J. Geophys. Res.*, **110**, D05108, doi:10.1029/2004JD004721.

Chen, Y.-L., and A. J. Nash, 1994: Diurnal variations of surface airflow and rainfall frequencies on the island of Hawaii. *Mon. Wea. Rev.*, **122**, 34–56, doi:10.1175/1520-0493(1994)122<0034: DVOSAA>2.0.CO;2.

Chu, P.-S., and J. D. Clark, 1999: Decadal variations of tropical cyclone activity over the central North Pacific. *Bull. Amer. Meteor. Soc.*, **80**, 1875–1881, doi:10.1175/1520-0477(1999)080<1875: DVOTCA>2.0.CO;2.

——, and H. Chen, 2005: Interannual and interdecadal rainfall variations in the Hawaiian Islands. *J. Climate*, **18**, 4796–4813, doi:10.1175/JCLI3578.1.

Cressman, G. P., 1959: An operational objective analysis system. *Mon. Wea. Rev.*, **87**, 367–374, doi:10.1175/1520-0493(1959)087<0367: AOOAS>2.0.CO;2.

Cretat, J. C., M. B. Pohl, and Y. Richard, 2011: Quantifying internal variability in a regional climate model: A case study for Southern Africa. *Climate Dyn.*, **37**, 1335–1356, doi:10.1007/s00382-011-1021-5.

Dee, D. P., and Coauthors, 2011: The ERA-Interim reanalysis: Configuration and performance of the data assimilation system. *Quart. J. Roy. Meteor. Soc.*, **137**, 553–597, doi:10.1002/qj.828.

Frazier, A. G., T. W. Giambelluca, H. F. Diaz, and H. L. Needham, 2016: Comparison of geostatistical approaches to spatially interpolate month-year rainfall for the Hawaiian Islands. *Int. J. Climatol.*, **36**, 1459–1470, doi:10.1002/joc.4437.

Fu, C., and Coauthors, 2005: Regional climate model intercomparison project for Asia. *Bull. Amer. Meteor. Soc.*, **86**, 257–266, doi:10.1175/BAMS-86-2-257.

Giambelluca, T. W., Q. Chen, A. G. Frazier, J. P. Price, Y.-L. Chen, P.-S. Chu, J. K. Eischeid, and D. M. Delparte, 2013: Online rainfall atlas of Hawai'i. *Bull. Amer. Meteor. Soc.*, **94**, 313–316, doi:10.1175/BAMS-D-11-00228.1.

——, and Coauthors, 2014: Evapotranspiration of Hawai'i. U.S. Army Corps of Engineers Final Rep., 168 pp. [Available online at http://evapotranspiration.geography.hawaii.edu/assets/files/PDF/ET%20Project%20Final%20Report.pdf.]

Guo, P., Y.-H. Kuo, S. V. Sokolovskiy, and D. H. Lenschow, 2011: Estimating atmospheric boundary layer depth using COSMIC radio occultation data. *J. Atmos. Sci.*, **68**, 1703–1713, doi:10.1175/2011JAS3612.1.

Harter, D. E. V., S. D. H. Irl, B. Seo, M. J. Steinbauer, R. Gillespie, K. A. Triantis, J.-M. Fernández-Palacios, and C. Beierkuhnlein, 2015: Impacts of global climate change on the floras of oceanic islands—Projections, implications and current knowledge. *Perspect. Plant Ecol. Evol. Syst.*, **17**, 160–183, doi:10.1016/j.ppees.2015.01.003.

Hartley, T. M., and Y.-L. Chen, 2010: Characteristics of summer trade wind rainfall over Oahu. *Wea. Forecasting*, **25**, 1797–1815, doi:10.1175/2010WAF2222328.1.

Hostetler, S. W., J. R. Alder, and A. M. Allan, 2011: Dynamically downscaled climate simulations over North America: Methods, evaluation and supporting documentation for users. U.S. Geological Survey Open-File Rep. 2011-1238, 64 pp. [Available online at http://pubs.usgs.gov/of/2011/1238/pdf/ofr20111238.pdf.]

Huffman, G. J., R. F. Adler, D. T. Bolvin, G. Gu, E. J. Nelkin, K. P. Bowman, E. F. Stocker, and D. B. Wolff, 2007: The TRMM Multisatellite Precipitation Analysis: Quasi-global, multiyear, combined-sensor precipitation estimates at fine scale. *J. Hydrometeor.*, **8**, 38–55, doi:10.1175/JHM560.1.

Kendon, E. J., N. M. Roberts, H. J. Fowler, M. J. Roberts, S. C. Chan, and C. A. Senior, 2014: Heavier summer downpours with climate change revealed by weather forecast resolution model. *Nat. Climate Change*, **4**, 570–576, doi:10.1038/nclimate2258.

Laprise, R., D. Caya, M. Giguère, G. Bergeron, H. Côté, J.-P. Blanchet, G. J. Boer, and N. A. McFarlane, 1998: Climate and climate change in western Canada as simulated by the Canadian

Regional Climate Model. *Atmos.–Ocean*, **36**, 119–167, doi:10.1080/07055900.1998.9649609.

Leong, J.-A., and Coauthors, 2014: Hawai'i and U.S. affiliated Pacific islands. *Climate Change Impacts in the United States: The Third National Climate Assessment*, J. M. Melillo, T.C. Richmond, and G. W. Yohe, Eds., U.S. Global Change Research Program, 537–556, doi:10.7930/J0W66HPM.

Lo, J. C.-F., Z.-L. Yang, and R. A. Pielke Sr., 2008: Assessment of three dynamical downscaling methods using the Weather Research and Forecasting (WRF) Model. *J. Geophys. Res.*, **113**, D09112, doi:10.1029/2007JD009216.

Lyons, S. W., 1982: Empirical orthogonal function analysis of Hawaiian rainfall. *J. Appl. Meteor.*, **21**, 1713–1729, doi:10.1175/1520-0450(1982)021<1713:EOFAOH>2.0.CO;2.

Mahoney, K., M. Alexander, J. D. Scott, and J. Barsugli, 2013: High-resolution downscaled simulations of warm-season extreme precipitation events in the Colorado Front Range under past and future climates. *J. Climate*, **26**, 8671–8689, doi:10.1175/JCLI-D-12-00744.1.

Mearns, L. O., and Coauthors, 2012: The North American Regional Climate Change Assessment Program: Overview of phase I results. *Bull. Amer. Meteor. Soc.*, **93**, 1337–1362, doi:10.1175/BAMS-D-11-00223.1.

Miguez-Macho, G., G. L. Stenchikov, and A. Robock, 2004: Spectral nudging to eliminate the effects of domain position and geometry in regional climate model simulations. *J. Geophys. Res.*, **109**, D13104, doi:10.1029/2003JD004495.

Morel, B., B. Pohl, Y. Richard, B. Bois, and M. Bessafi, 2014: Regionalizing rainfall at very high resolution over La Réunion Island using a regional climate model. *Mon. Wea. Rev.*, **142**, 2665–2686, doi:10.1175/MWR-D-14-00009.1.

Pérez, J. C., J. P. Díaz, A. González, J. Expósito, F. Rivera-López, and D. Taima, 2014: Evaluation of WRF parameterizations for dynamical downscaling in the Canary Islands. *J. Climate*, **27**, 5611–5631, doi:10.1175/JCLI-D-13-00458.1.

Prein, A. F., and Coauthors, 2015: A review on regional convection-permitting climate modeling: Demonstrations, prospects, and challenges. *Rev. Geophys.*, **53**, 323–361, doi:10.1002/2014RG000475.

Rasmussen, R., and Coauthors, 2014: Climate change impacts on the water balance of the Colorado headwaters: High-resolution regional climate model simulations. *J. Hydrometeor.*, **15**, 1091–1116, doi:10.1175/JHM-D-13-0118.1.

Reynolds, R. W., C. L. Gentemann, and G. K. Corlett, 2010: Evaluation of AATSR and TMI satellite SST data. *J. Climate*, **23**, 152–165, doi:10.1175/2009JCLI3252.1.

Rienecker, M. M., and Coauthors, 2011: MERRA: NASA's Modern-Era Retrospective Analysis for Research and Applications. *J. Climate*, **24**, 3624–3648, doi:10.1175/JCLI-D-11-00015.1.

Rummukainen, M., 2010: State-of-the-art with regional climate models. *Wiley Interdiscip. Rev.: Climate Change*, **1**, 82–96, doi:10.1002/wcc.8.

Schroeder, T. A., 1993: Climate controls. *Prevailing Trade Winds: Weather and Climate in Hawai'i*, M. Sanderson, Ed., University of Hawai'i Press, 12–36.

——, B. Kilonsky, and B. Meisner, 1977: Diurnal variation in rainfall and cloudiness. Water Resources Research Center Tech. Rep. 112, 67 pp.

Sen Roy, S., and R. C. Balling, 2004: Analysis of Hawaiian diurnal rainfall patterns. *Theor. Appl. Climatol.*, **79**, 209–214, doi:10.1007/s00704-004-0075-2.

Skamarock, W. C., and Coauthors, 2008: A description of the Advanced Research WRF version 3. NCAR Tech. Note NCAR/TN-475+STR, 113 pp, doi:10.5065/D68S4MVH.

Sokolovskiy, S., Y.-H. Kuo, C. Rocken, W. S. Schreiner, D. Hunt, and R. A. Anthes, 2006: Monitoring the atmospheric boundary layer by GPS radio occultation signals recorded in the open-loop mode. *Geophys. Res. Lett.*, **33**, L12813, doi:10.1029/2006GL025955.

Taylor, K. E., R. J. Stouffer, and G. A. Meehl, 2012: An overview of CMIP5 and the experiment design. *Bull. Amer. Meteor. Soc.*, **93**, 485–498, doi:10.1175/BAMS-D-11-00094.1.

Wang, Y., L. R. Leung, J. L. McGregor, D.-K. Lee, W.-C. Wang, Y.-H. Ding, and F. Kimura, 2004: Regional climate modeling: Progress, challenges and prospects. *J. Meteor. Soc. Japan*, **82**, 1599–1628, doi:10.2151/jmsj.82.1599.

Xie, F., D. L. Wu, C. O. Ao, A. J. Mannucci, and E. R. Kursinski, 2012: Advances and limitations of atmospheric boundary layer observations with GPS occultation over southeast Pacific Ocean. *Atmos. Chem. Phys.*, **12**, 903–918, doi:10.5194/acp-12-903-2012.

Zhang, C. X., Y. Wang, and K. Hamilton, 2011: Improved representation of boundary layer clouds over the southeast Pacific in WRF-ARW using a modified Tiedtke cumulus parameterization scheme. *Mon. Wea. Rev.*, **139**, 3489–3513, doi:10.1175/MWR-D-10-05091.1.

——, ——, A. Lauer, and K. Hamilton, 2012a: Configuration and evaluation of the WRF Model for the study of Hawaiian regional climate. *Mon. Wea. Rev.*, **140**, 3259–3277, doi:10.1175/MWR-D-11-00260.1.

——, ——, ——, ——, and F. Xie, 2012b: Cloud base and top heights in the Hawaiian region determined with satellite and ground-based measurements. *Geophys. Res. Lett.*, **39**, L15706, doi:10.1029/2012GL052355.